CrossMark

The Green Monster Hiding in Front of Cas A: JWST Reveals a Dense and Dusty Circumstellar Structure Pockmarked by Ejecta Interactions

Ilse De Looze[1], Dan Milisavljevic[2,3], Tea Temim[4], Danielle Dickinson[2], Robert Fesen[5], Richard G. Arendt[6,7,8], Jeremy Chastenet[1], Salvatore Orlando[9], Jacco Vink[10,11], Michael J. Barlow[12], Florian Kirchschlager[1], Felix D. Priestley[13], John C. Raymond[14], Jeonghee Rho[15,16], Nina S. Sartorio[1], Tassilo Scheffler[1], Franziska Schmidt[12], William P. Blair[17], Ori Fox[18], Christopher Fryer[19,20,21,22], Hans-Thomas Janka[23], Bon-Chul Koo[24], J. Martin Laming[25], Mikako Matsuura[13], Dan Patnaude[14], Mónica Relaño[26], Armin Rest[27,28], Judy Schmidt[29], Nathan Smith[30], and Niharika Sravan[31]

[1] Sterrenkundig Observatorium, Ghent University, Krijgslaan 281—S9, B-9000 Gent, Belgium
[2] Purdue University, Department of Physics and Astronomy, 525 Northwestern Avenue, West Lafayette, IN 47907, USA
[3] Integrative Data Science Initiative, Purdue University, West Lafayette, IN 47907, USA
[4] Princeton University, 4 Ivy Lane, Princeton, NJ 08544, USA
[5] Department of Physics and Astronomy, Dartmouth College, 6127 Wilder Lab, Hanover, NH 03755, USA
[6] Center for Space Sciences and Technology, University of Maryland, Baltimore County, Baltimore, MD 21250, USA
[7] NASA/GSFC, 8800 Greenbelt Road, Code 665, Greenbelt, MD 20771, USA
[8] Center for Research and Exploration in Space Science and Technology, NASA/GSFC, Greenbelt, MD 20771, USA
[9] INAF—Osservatorio Astronomico di Palermo, Piazza del Parlamento 1, 90134 Palermo, Italy
[10] Anton Pannekoek Institute for Astronomy & GRAPPA, University of Amsterdam, Science Park 904, 1098 XH Amsterdam, The Netherlands
[11] SRON Netherlands Institute for Space Research, Niels Bohrweg 4, 2333 CA Leiden, The Netherlands
[12] Department of Physics and Astronomy, University College London, Gower Street, London WC1E 6BT, UK
[13] Cardiff Hub for Astrophysical Research and Technology (CHART), School of Physics & Astronomy, Cardiff University, The Parade, Cardiff CF24 3AA, UK
[14] Center for Astrophysics |Harvard & Smithsonian, 60 Garden Street, Cambridge, MA 02138, USA
[15] SETI Institute, 339 Bernardo Avenue, Suite 200, Mountain View, CA 94043, USA
[16] Department of Physics and Astronomy, Seoul National University, Gwanak-ro 1, Gwanak-gu, Seoul, 08826, Republic of Korea
[17] The William H. Miller III Department of Physics and Astronomy, Johns Hopkins University, 3400 North Charles Street, Baltimore, MD 21218, USA
[18] Space Telescope Science Institute, 3700 San Martin Drive, Baltimore, MD 21218, USA
[19] Center for Theoretical Astrophysics, Los Alamos National Laboratory, Los Alamos, NM 87545, USA
[20] Department of Astronomy, The University of Arizona, Tucson, AZ 85721, USA
[21] Department of Physics and Astronomy, The University of New Mexico, Albuquerque, NM 87131, USA
[22] Department of Physics, The George Washington University, Washington, DC 20052, USA
[23] Max-Planck-Institut für Astrophysik, Karl-Schwarzschild-Str. 1, 85748, Garching, Germany
[24] Department of Physics and Astronomy, Seoul National University, Seoul 08861, Republic of Korea
[25] Space Science Division, Code 7684, Naval Research Laboratory, Washington, DC 20375, USA
[26] Dept. Física Teórica y del Cosmos, Universidad de Granada, 18071, Granada, Spain
[27] Space Telescope Science Institute, Baltimore, MD 21218, USA
[28] Department of Physics and Astronomy, The Johns Hopkins University, Baltimore, MD 21218, USA
[29] Astrophysics Source Code Library, Michigan Technological University, 1400 Townsend Drive, Houghton, MI 49931, USA
[30] Steward Observatory, University of Arizona, 933 North Cherry Avenue, Tucson, AZ 85721, USA
[31] Department of Physics, Drexel University, Philadelphia, PA 19104, USA

Abstract

JWST observations of the young Galactic supernova remnant Cassiopeia A revealed an unexpected structure seen as a green emission feature in colored composite MIRI F1130W and F1280W images—hence dubbed the Green Monster—that stretches across the central parts of the remnant in projection. Combining the kinematic information from NIRSpec and the MIRI Medium Resolution Spectrograph with the multiwavelength imaging from NIRCam and MIRI, we associate the Green Monster with circumstellar material (CSM) that was lost during an asymmetric mass-loss phase. MIRI images are dominated by dust emission, but their spectra show emission lines from Ne, H, and Fe with low radial velocities indicative of a CSM nature. An X-ray analysis of this feature in a companion paper supports its CSM nature and detects significant blueshifting, thereby placing the Green Monster on the nearside, in front of the Cas A supernova remnant. The most striking features of the Green Monster are dozens of almost perfectly circular $1''$–$3''$ sized holes, most likely created by interaction between high-velocity supernova ejecta material and the CSM. Further investigation is needed to understand whether these holes were formed by small 8000–10,500 km s^{-1} N-rich ejecta knots that penetrated and advanced out ahead of the remnant's 5000–6000 km s^{-1} outer blast wave or by narrow ejecta fingers that protrude into the forward-shocked CSM. The detection of the Green Monster provides further evidence of the highly asymmetric mass loss that Cas A's progenitor star underwent prior to its explosion.

Unified Astronomy Thesaurus concepts: Supernova remnants (1667); Core-collapse supernovae (304); Circumstellar dust (236); Ejecta (453); Stellar mass loss (1613)

1. Introduction

Cassiopeia A (Cas A) is one of the best-studied core-collapse supernova remnants (SNRs) in our Galaxy due to both its youth and its relatively short distance of ∼3.4 kpc (J. E. Reed et al. 1995; A. Alarie et al. 2014). Detailed studies of Cas A using multiwavelength imaging and spectroscopic campaigns have given us unprecedented insights into supernova (SN) explosion asymmetries (R. A. Fesen 2001; U. Hwang et al. 2004; B. W. Grefenstette et al. 2014; D. Milisavljevic & R. A. Fesen 2015), dust formation in the SN ejecta (J. Rho et al. 2008; M. J. Barlow et al. 2010; A. Bevan et al. 2017; I. De Looze et al. 2017; F. D. Priestley et al. 2022), the subsequent destruction by the reverse shock (C. Biscaro & I. Cherchneff 2016; M. Bocchio et al. 2016; E. R. Micelotta et al. 2016; F. Kirchschlager et al. 2019, 2023), and particle acceleration in SN forward and reverse shocks (E. A. Helder & J. Vink 2008).

While no firm records exist of the sighting of the explosion of Cas A nearly 350 yr ago (J. R. Thorstensen et al. 2001; B.C. Koo & C. Park 2017), the postexplosion classification of Cas A as a Type IIb SN based on light echo spectra (O. Krause et al. 2008; A. Rest et al. 2008, 2011) suggests that the Cas A progenitor experienced significant mass loss, having shed most of its hydrogen layer prior to explosion. Such heavy mass loss from a massive progenitor star (15–25 $M_\odot$; R. A. Fesen et al. 1987; R. A. Fesen 2001; P. A. Young et al. 2006) has possibly occurred due to interactions with a binary companion (R. A. Chevalier & J. Oishi 2003; P. A. Young et al. 2006; O. Krause et al. 2008; K. E. Weil et al. 2020). However, deep searches have not yet resulted in the detection of a companion star (C. S. Kochanek 2018; W. E. Kerzendorf et al. 2019), leaving the possibility that the binary star is a faint low-mass dwarf or that the two stars merged prior to the SN explosion (e.g., K. Nomoto et al. 1993).

Studying the mass-loss history of Cas A—with constraints on the timing, the rate, and the asymmetry of the mass loss—can give important insights into the preexplosion conditions. There is evidence in the literature for several mass-loss phases. Diffuse emission clouds about 10–20 pc to the north, east, and northwest of the explosion center detected in optical data are thought to arise from a slow (10 km s^{-1}) red supergiant (RSG) wind (K. E. Weil et al. 2020). Studies of the X-ray ejecta knots are consistent with Cas A expanding into a slow RSG wind (J. M. Laming & U. Hwang 2003; U. Hwang & J. M. Laming 2009) with a relatively high density (∼1 cm^{-3}) for the preshock wind material (J.-J. Lee et al. 2014) at the current outer radius (∼3 pc) of Cas A. Faint dust emission was detected with Spitzer and Herschel roughly 2–3 pc north and east of the explosion center (M. J. Barlow et al. 2010; R. G. Arendt et al. 2014) and corresponds to the infrared counterpart of the X-ray emission that was thought to originate from a tenuous slow RSG wind.

With the advent of the James Webb Space Telescope (JWST), we can now map out the details of the circumstellar material (CSM) dust structures shocked by the SN blast wave (D. Milisavljevic et al. 2024). The circumstellar dust emission detected north, east, and west of Cas A stands out as diffuse red emission around the periphery of the shocked ejecta shell in the JWST multicolor image (see Figure 1). Although the coverage toward the south does not extend much beyond 2 pc, filamentary structures trace out CSM that seems to follow the onset of an arc-like structure populated with dense circumstellar clumps often referred to as quasi-stationary flocculi (QSFs; see Figure 8).

The nature of these QSFs, first identified in optical images starting in the early 1950s (W. Baade & R. Minkowski 1954; R. Minkowski 1959; S. van den Bergh & W. W. Dodd 1970; M. Peimbert & S. van den Bergh 1971; S. van den Bergh 1971; K. Kamper & S. van den Bergh 1976), is less clear. QSFs are generally considered to be dense, pre-SN CSM knots with relatively low radial velocities of between −500 and +100 km s^{-1} (S. van den Bergh & K. Kamper 1985; A. Alarie et al. 2014; B.-C. Koo et al. 2018), which led to them being called "quasi-stationary" compared to Cas A's fast-moving knots (FMKs) of SN ejecta. Detailed studies of optical and near-infrared (NIR) data suggest that these QSFs have a high density (10^3–10^4 cm^{-3}; B.-C. Koo et al. 2020), requiring recent (forward) shock interaction to make them detectable at optical and NIR wavelengths.

The He and N enrichment of QSFs (R. A. Chevalier & R. P. Kirshner 1978; S. A. Lamb 1978; B.-C. Koo et al. 2023) is suggestive of CNO-processed CSM originating from the H-burning shell of the progenitor and must have been generated at an evolved stage of stellar evolution for elements near the H-burning shell to reach the surface, hence after a significant portion of the hydrogen envelope was stripped. Indeed, proper motions of several QSFs suggest that the material was lost by the progenitor star roughly 10^4 yr prior to explosion (M. Peimbert & S. van den Bergh 1971; K. Kamper & S. van den Bergh 1976; R. A. Chevalier & R. P. Kirshner 1978; S. van den Bergh & K. Kamper 1985). However, this value should be considered with caution given that recent interaction with Cas A's forward shock front may have influenced the QSFs' currently observed motion.

It is unclear how these dense circumstellar clumps with unshocked densities of ∼1000 cm^{-3} formed in the first place. In one scenario, the QSFs originate from hydrodynamical instabilities that occurred in a dense shell of the RSG wind that got compressed by a fast wind in the final blue/yellow supergiant or Wolf–Rayet phase of the progenitor prior to the explosion. The dense remainders of this RSG wind-driven shell could be the QSFs shocked by the SN blast wave that we observe today.

However, the QSFs are distributed asymmetrically around the remnant and do not seem to follow a shell structure (A. Alarie et al. 2014; B.-C. Koo et al. 2018). It has been suggested that QSFs could be dense clumps, formed as overdensities in a smooth RSG wind, rather than the fragments of a disrupted circumstellar shell (R. A. Chevalier & J. Oishi 2003). The QSFs are also reminiscent of the slow N-rich condensations around η Carinae (N. Smith & J. A. Morse 2004), raising the possibility that they may have resulted instead from episodic mass loss during binary interaction.

Studies of the X-ray properties of shocked outer ejecta knots suggest that there may have been a brief post-RSG phase that created a small (0.2–0.3 pc) low-density cavity around Cas A (U. Hwang & J. M. Laming 2009). The presence of the northeast jet constrains the duration of such a high-velocity wind to significantly less than 10,000 yr (K. M. Schure et al. 2008). Such a low-density cavity could have formed from a tenuous fast wind originating from a Wolf–Rayet star or a yellow supergiant (K. E. Weil et al. 2020). But a Wolf–Rayet star scenario may be considered less likely due to the difficulty of explaining the formation of QSFs by a Wolf–Rayet wind
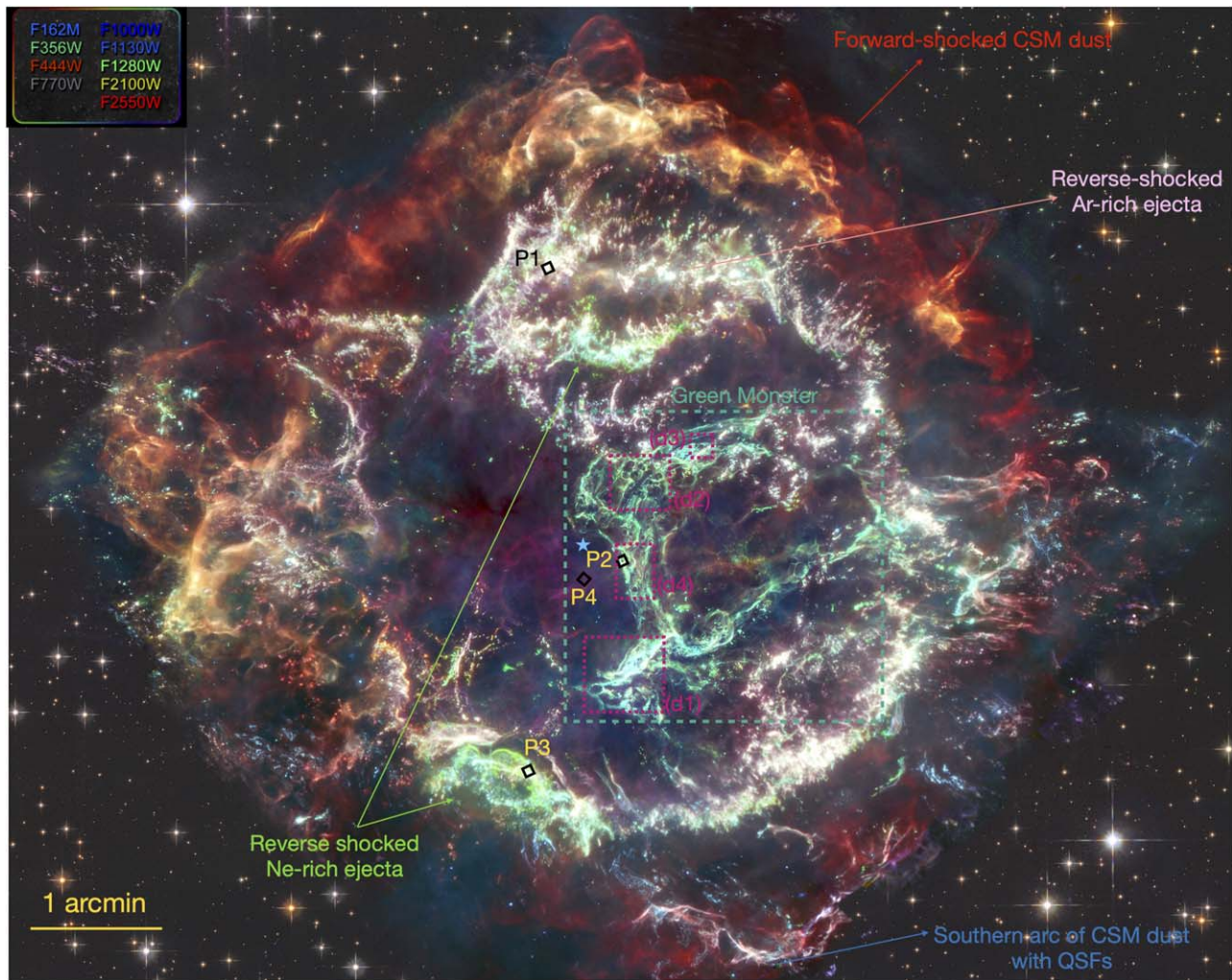
Figure 1. Multicolor JWST/NIRCam and MIRI image of Cas A adapted from D. Milisavljevic et al. (2024) with the locations of the four MIRI MRS pointings overlaid as black squares. The green rectangular region marks the position of the GM, which is shown enlarged in Figure 2, whereas the magenta rectangles outline several regions of interest of which we provide a multiwavelength view in Figure 4. The explosion center is highlighted with a blue star. Beyond the coverage of the JWST images, we use a 2023 epoch HST image to fill in the emission in the background. The legend outlines the representation for each color in this multicolor image. The prominent green emission observed from the GM originates mostly from the MIRI/F1280W filter with contributions from MIRI/F1130W. The GM emission is not to be confused with the reverse-shocked Ne-rich ejecta visible in light green (representative of the bright Ne line in the F1280W filter). The reverse-shocked Ar-rich ejecta are instead mostly colored pink and white thanks to the Ar line contributions to the F770W filter and the dust continuum emission with a characteristic 21 μm peak significantly contributing to the F2100W and F2550W images. The forward-shocked CSM dust in the north, east, and west is colored red and orange owing to the circumstellar dust emission peaking in the F2100W and F2550W filters.

(B. van Veelen et al. 2009) and due to the presence of H in the light echo spectra suggesting that some H was left after the mass loss (O. Krause et al. 2008; A. Rest et al. 2008, 2011). In general, Wolf–Rayet stars tend to be associated with more massive ($>40\,M_\odot$) progenitor stars (R. M. Humphreys et al. 1985), which would be at odds with the currently predicted progenitor mass (15–$25\,M_\odot$) of Cas A.

The spatially varying velocities of the reverse shock across the remnant and the backward motion of the reverse shock toward the west (R. Fesen et al. 2019; J. Vink et al. 2022) also suggest that the forward shock initially traversed a lopsided cavity. However, the backward motion of the reverse shock could also be explained through the interaction of the SN blast wave with a partial dense circumstellar shell ≈ 200 yr after the explosion (S. Orlando et al. 2022; J. Vink et al. 2022). The presence of such a fast wind during a brief blue or yellow supergiant or Wolf–Rayet phase has been suggested from both observations and simulations (U. Hwang & J. M. Laming 2009;

B.-C. Koo et al. 2020; K. E. Weil et al. 2020; S. Orlando et al. 2022; J. Vink et al. 2022), but again the connection of this heavy mass-loss episode with the presence of QSFs and other mass-loss phases remains unclear.

JWST (J. P. Gardner et al. 2023; J. Rigby et al. 2023) is an ideal facility to map out the shocked and unshocked ejecta structures in Cas A (D. Milisavljevic et al. 2024) and to study its pre-SN mass-loss history. The shock-heated CSM warm dust emission lights up at mid-infrared wavelengths (see Figure 1), and the [Fe II] 1.644 μm line emission probed with NIRCam allows one to study both dense shocked CSM and shocked ejecta clumps (B.-C. Koo et al. 2024, in preparation). The JWST data, furthermore, reveal the spatial distribution of CO molecules that reformed in the ejecta after reverse shock processing (J. Rho et al. 2024) and provide unique insights into the chemical diversity of SN dust formation (T. Temim et al. 2024, in preparation).

Each new telescope facility observing Cas A made surprising discoveries, contributing to our understanding of SN explosion physics and pre-SN mass loss. One of the most striking features of the new JWST/NIRCam and MIRI observations of Cas A (see Figure 1) is a prominent structure dubbed the "Green Monster"[32] (hereafter GM) due to its green color in the multicolor press release image of Cas A, shown in Figure 1. The emission from this region is particularly bright in the MIRI F1130W and F1280W filters and dominates the central region of the SNR. Apart from its color, the GM stands out for hosting peculiar circular structures. In this paper, we use MIRI Medium Resolution Spectrograph (MRS) and NIRSpec observations of one specific targeted ring structure in the GM—in addition to NIRCam and MIRI photometric mapping of the entire GM structure—to study the nature of the mid-infrared emitting material.

The observational details are described in Section 2. The observational characteristics of the GM as seen by the JWST are presented in Section 3. The nature of the GM emission is discussed in Section 4, along with several scenarios that can account for the creation of the holes and rings. We discuss how the GM's structure fits into the overall mass-loss history of Cas A (Section 5) before concluding (Section 6). Appendices A.1 and A.2 provide a detailed explanation of how the line velocity profiles and maps were obtained.

2. Observations

2.1. JWST/MIRI and JWST/NIRCam Imaging Data

The Galactic SNR Cas A was observed with JWST/MIRI (G. S. Wright et al. 2023) and JWST/NIRCam (M. J. Rieke et al. 2023) during 2022 August and 2022 November, covering the entire remnant and part of its surroundings, as part of the Cycle 1 program GO01947 (PI: D. Milisavljevic). A return visit was required for MIRI to cover gaps between the detector footprints, and this took place in 2022 November. A full description of the observational details and data reduction pipeline is given in D. Milisavljevic et al. (2024). We briefly summarize the most important information here. We obtained data in a 3×5 (fields of view) mosaic for all MIRI filters—except for the F1500W filter[33]—providing us with good coverage of the mid-infrared spectral energy distribution (SED). We used the FASTR1 readout mode, with eight groups and one integration per exposure and a four-point dither pattern, amounting to a total exposure time of 88.8 s per individual field. A dedicated background observation was obtained, and the background emission was subtracted during level 2 pipeline processing (except for the F770W, F1000W, F1130W, and F1280W filters, which show highly variable background emission levels). Aside from standard data reduction procedures—but skipping the use of the `tweakreg` and `skymatch` steps—the regular and return visits were combined into a single mosaic after applying corrections for astrometric offsets using Gaia DR3 catalogs based on the output from the JWST HST Alignment Tool (A. Rest et al. 2023). These astrometric corrections were fine-tuned on the highest-resolution F560W image and applied to the other MIRI filters. Due to small-scale spatial variations in the mid-infrared

interstellar dust emission in the background of Cas A (e.g., I. De Looze et al. 2017), we required a separate background subtraction routine to match the zero levels of all eight MIRI images. Note that we did not subtract the variable background emission, which would require detailed modeling efforts to disentangle the different sources of emission (interstellar, circumstellar, and ejecta line and dust emission). Instead, we selected regions with no obvious background emission outside of the remnant and scaled all the MIRI images to have zero flux within these regions.

The JWST/NIRCam observations were designed to study the [Fe II] 1.644 μm line and the 4.5 μm CO fundamental band using one medium (F162M) and two wide (F356W, F444W) filters, respectively. These observations are discussed and analyzed in more detail in J. Rho et al. (2024) and B.-C. Koo et al. (2024, in preparation). In brief, the remnant was covered with a 3×1 (fields of view) mosaic using the BRIGHT1 readout pattern with seven groups and one integration per exposure. The total exposure time was 1675 s for a total of 12 dithers per field using the 3TIGHT primary dithers, including four subpixel dithers. The exposure time was doubled for the F162M filter since this short-wavelength camera filter was covered during both of the F356W and F444W observations with the long-wavelength camera. The image processing for NIRCam was done using the calibration pipeline (v 1.8.4) with the calibration reference data system v 11.16.14, in a similar way as was done for the MIRI imaging data.

The spatial resolution (expressed in terms of the FWHM of the point-spread function, PSF) achieved with NIRCam (0″055, 0″116, and 0″145 for the F162M, F356W, and F444W filters) and MIRI (ranging from 0″207 for F560W to 0″803 for F2550W) corresponds to physical scales ranging between 190 au (2.8×10^{15} cm) and 2700 au (4.1×10^{16} cm) if we assume a distance to Cas A of 3.4 kpc. NIRCam filters are dominated by synchrotron emission and line emission, mostly from the [Fe II] 1.644 μm line and the CO fundamental band at 4.6 μm, but fainter lines ([Si I] 1.645 μm, [Si IX] 3.94 μm, and [Mg IV] 4.49 μm) and emission from polycyclic aromatic hydrocarbons and hot carbonaceous dust can also have nonnegligible contributions in certain regions. While the F560W image is largely dominated by synchrotron emission, all other MIRI filters have a stronger contribution from dust emission originating from different sources (circumstellar, interstellar, and ejecta dust). Various MIRI filters also have nonnegligible contributions from line emission (see Table 1 in D. Milisavljevic et al. 2024 for an overview). Most of these lines (e.g., [Ar II] 6.99 μm, [Ar III] 8.99 μm, [S IV] 10.51 μm, [Ne II] 12.81 μm, [S III] 18.71 μm, and [O IV] 25.89 μm) originate from the SN ejecta, but some lines ([Ne II] 12.81 μm, [Ne III] 15.56 μm, and H$_2$ (0,0) S(1) 17.03 μm) may have a circum- or interstellar origin.

2.2. JWST/MIRI MRS and JWST/NIRSpec Spectroscopic Data

Four different regions of interest were zoomed into with JWST's spectroscopic instrumentation (see Figure 1). One deep drilling was done of a central region in the unshocked ejecta (P4); these observations are discussed in more detail in D. Milisavljevic et al. (2024). Three other pointings target reverse-shocked ejecta knots in the northeast with bright Ar line emission (P1), a hole with a surrounding ring in the GM structure (P2), and a reverse-shocked region in the south with bright Ne emission and the presence of bright warm CO gas

---

[32] Cas A's GM was named after the tall, imposing green wall in the left field of Fenway Park, home of the Boston Red Sox baseball team.

[33] We obtained partial coverage for the F1500W filter from simultaneous MIRI imaging during the MRS observations.

(P3; see Figure 1). In this paper, we will present the spectroscopic observations of one circular ring structure in the GM (P2) along with the photometric observations of the entire GM.

Each of these regions was covered with the MIRI MRS and the NIRSpec integral field unit (IFU)[34] instruments. For specific details on the MIRI MRS data reduction, we refer to the survey paper (D. Milisavljevic et al. 2024). Here we briefly summarize the spectroscopic observations for position P2, which were taken in 2022 November. MRS observations of three different gratings (short, medium, and long) guaranteed coverage of the full wavelength range between 4.9 and 27.9 μm. The FASTR1 readout mode was used, and a four-point dithering scheme for extended sources was adopted. Each exposure in a given grating setting and wavelength range (MRSSHORT or MRSLONG) consisted of 50 groups and four integrations (due to the four-point dithering), resulting in an exposure time of 555 s. Simultaneous imaging was done in the F560W, F770W, and F1500W filters. In addition to the standard data reduction pipeline (we used v 1.11.0), the `jwst.residual_fringe.ResidualFringeStep` was used, and a dedicated background was subtracted using the master background subtraction method. The 12 individual spectra from the different channel and grating combinations were additively scaled to obtain a smooth stitched spectrum. To check the astrometry, we integrated the line-free continuum in various MIRI broadband filters and compared these images to the MIRI mosaics, which have been anchored to the Gaia DR3 targets. We found an offset between the MRS data and the MIRI images of $\sim0\rlap{.}''25$ and corrected the world coordinate system of the MRS data cubes for this offset. Figure 3 (top panel) shows a global extraction of the mid-infrared emission in the dedicated MRS observations of position P2. It is immediately evident from the spectrum that several emission lines—in particular the [S IV] 10.51 μm, [Ne II] 12.81 μm, and [O IV] 25.89 μm lines—have multiple velocity components corresponding to different physical regions along the line of sight.

The NIRSpec IFU data were taken during 2022 November and December with the medium-resolution grating G395M ($R \sim 1000$) and filter F290LP covering the 2.87–5.10 μm wavelength range. Two different exposures were taken—one with and one without leakcal—to allow for corrections for spectral contamination from malfunctioning open Micro-Shutter Assembly (MSA) shutters in postprocessing. Each exposure consisted of 15 groups and four integrations due to the four-point dithering scheme, resulting in a 933.69 s exposure time. The NRSIRS2RAPID readout pattern was used. The NIRSpec data were processed with the standard data reduction pipeline (calibration files v 1.11.4). The spectrum extracted from a $2\rlap{.}''5 \times 2\rlap{.}''5$ box centered on this specific ring in the GM is shown in Figure 3 (bottom panel). The detected lines are quite faint, making the line identification more difficult. The Brα line is near zero velocity, whereas the other lines (i.e., [Mg VIII], [Mg IV], He II 7–6, and He II 8–7) appear to be emitted from a high-velocity ($v = 5000$ km s^{-1}) component. Unconfirmed line identifications have been indicated with a question mark.

_____
[34] For the long exposure of the unshocked ejecta, the NIRSpec fixed slit mode was used instead of the IFU.

2.3. Ancillary Data Products

We use Hubble Space Telescope (HST) data from the HST Advanced Camera for Surveys (ACS) WFC program "A Multi-Bandpass ACS Survey of Cassiopeia A: Keeping Up with its Rapidly Evolving Structure" (PI: R. Fesen) targeting Cas A in 2022 December and 2023 May using different filters (F450W, F625W, F775W, and F850LP) to distinguish between O-Ne-rich and S-Ar-Ca-rich ejecta in Cas A. In this paper, we made use of the ACS/WFC F625W image that is sensitive to Hα line emission from CSM and to the emission from the [S II] 6716, 6731 Å doublet originating from S-rich ejecta.

3. Observational Characteristics of the GM

In this section, we review observations that will best indicate the nature of the GM in Section 4.

3.1. Morphology of the GM

Figure 1 shows a multicolor MIRI+NIRCam image of Cas A highlighting the complexity of this SNR system. The red and orange clouds outside of the main remnant correspond to the material that was lost by the progenitor star before its explosion and is currently being overrun by the SN blast wave. The magenta, pink, and white colors reveal clumpy ejecta knots that have been shocked by the remnant's reverse shock. This reverse-shocked material also outlines the fast-moving ejecta that form the jet in the east and the protrusion of the ring in the west.

Some of the ejecta is particularly rich in neon with prominent emission lines in the MIRI/F1280W filter, which makes these regions appear green. Toward the center, the green colors (representative of the emission in the MIRI/F1130W and F1280W filters) reveal a new GM structure that is mostly located within the borders of the SNR. Using Spitzer data, R. G. Arendt et al. (2014) identified the brightest part of the GM as the south spot dust and speculated that it could originate from circum- or interstellar material. An outline of the fainter GM emitting regions is also shown in Figure 4 of that paper, but back then it was not yet identified as belonging to the same structure. Hints of emission from the GM are also seen in earlier Infrared Space Observatory data (P. O. Lagage et al. 1996), suggesting that the GM has been bright at mid-infrared wavelengths for at least ~30 yr.

Zooming into this new structure, we unexpectedly discovered numerous partial or complete circular structures ("holes") across much of the GM. Figure 2 showcases multicolor MIRI images that provide an enlarged view of these circular structures. From this high-resolution view, most of these features correspond to regions empty, or nearly so, of any infrared emission surrounded by thin circular rings of enhanced emission some $0\rlap{.}''25$–$0\rlap{.}''5$ thick.

In an attempt to characterize these circular structures, we first manually identified them in the JWST/MIRI F1130W image and then measured the range of typical sizes of these structures. From our visual inspection, we identified more than two dozen circular structures with typical sizes ranging between $\sim1''$ and $3''$ (~0.015–0.05 pc) in diameter. While some ringlike features have diameters that exceed $3''$, most of these are faint or partial and thus more difficult to characterize due to their fainter and/or partial appearance. The nearly perfect circular shape of a large fraction of these holes does not leave many
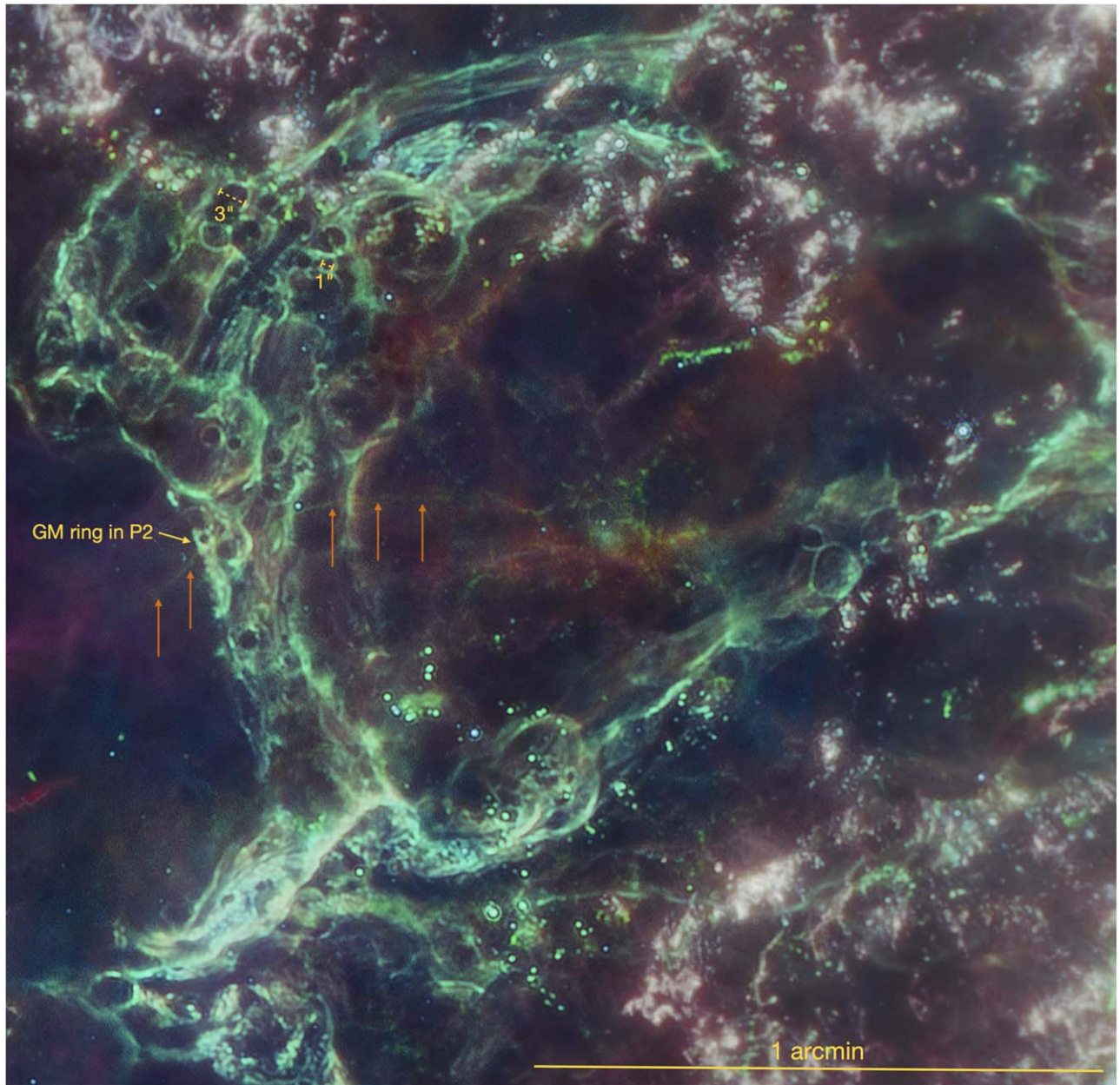
Figure 2. This JWST multicolor image presents the main GM region applying the same color scheme for NIRCam and MIRI images as used in Figure 1. The most striking features are dozens of circular holes speckled across the GM, with sizes ranging between ≈1″ and 3″ (see the scale bars for some of the holes in the top). The orange arrows point to a very faint and curved ∼1 pc long ejecta filament that seems to run up against the base of a ring structure with targeted MRS observations in position P2 (see also Figure 1). We argue that the ejecta interaction with a reverse shock at this specific location is coincidental.

possible scenarios to explain their creation, a topic that we will address in Section 4.

The dust emission that dominates the GM's emission in the MIRI images almost never traces out a complete ring. Instead, we see that the partial ring structures are characterized by small regions of bright emission, which could indicate that these are local density enhancements in the GM rings or that the dust is locally heated to higher temperatures, boosting its emission. Similar to these bright enhancements in the circular structures, the GM emission is dominated by filamentary and clumpy structures of which some are a lot brighter than the surrounding regions.

While the GM structure was first identified from the JWST/ MIRI images, the JWST/NIRCam images also reveal some traces of the GM emission. In the NIRCam images, a diffuse emission component traces nonthermal synchrotron radiation, which is most visible in the NIRCam/F444W image (see Figure 4). The dominant emission in the NIRCam/F162M image originates from bright clumps that trace [Fe II] 1.644 μm line emission with a possible nonnegligible contribution from synchrotron emission (see Appendix A.2). While the NIR-Cam/F162M filter covers both the [Fe II] 1.644 μm and [Si I] 1.645 μm emission lines, B.-C. Koo et al. (2018) have argued using previous ground-based narrowband imaging that the diffuse emission component likely originates from [Si I] 1.645 μm line emission. The [Fe II] 1.644 μm line emission was found to be more clumped and likely originates from shocked material, which is also consistent with the detection of Hα 0.656 μm line emission from several Fe-bright CSM clumps (see the second column in Figure 4).
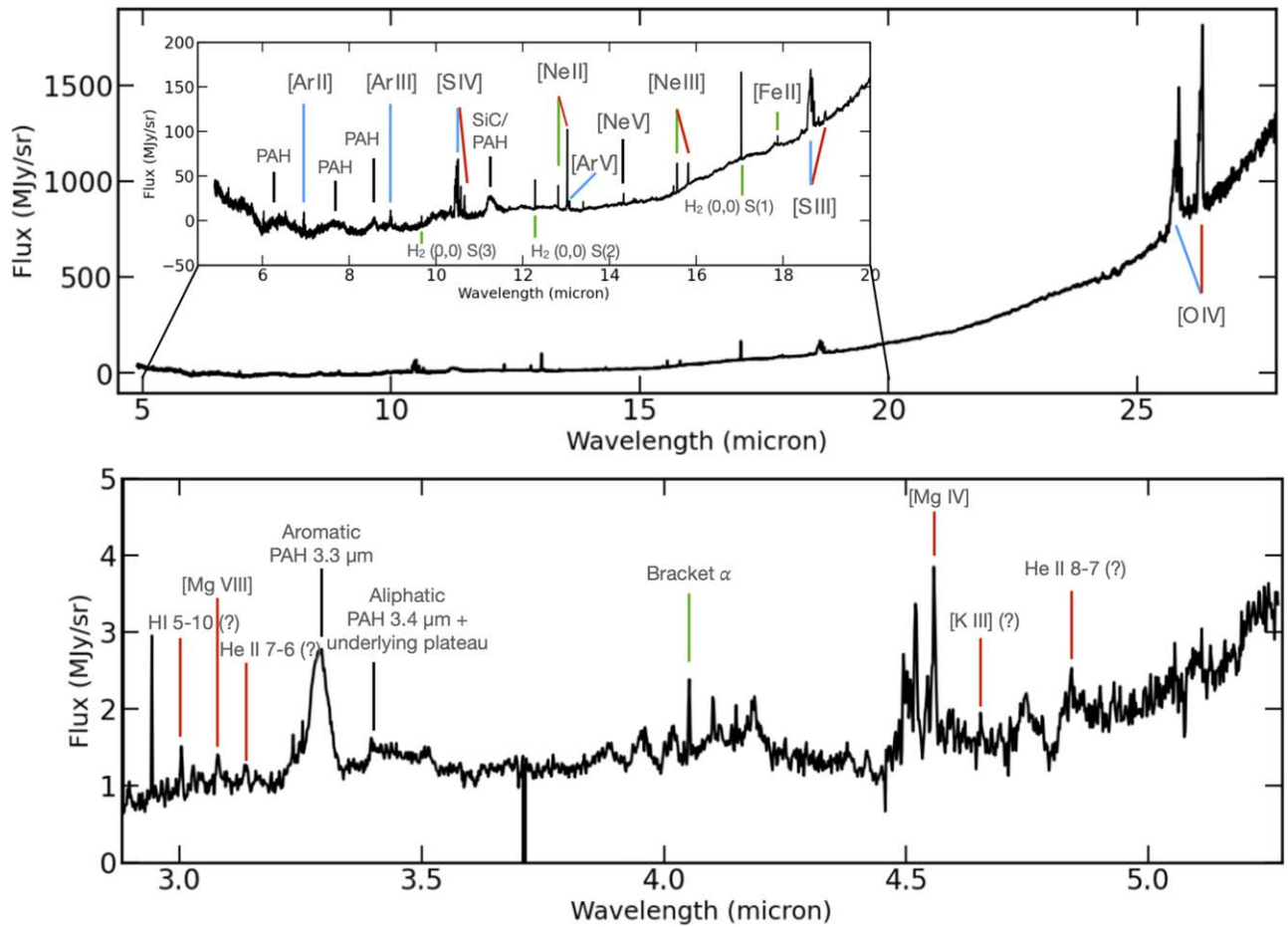
Figure 3. Total integrated MIRI MRS and NIRSpec spectra for one specific ring in the GM (position P2) with line identifications, some of which remain uncertain. The colors indicate whether the line emission is mostly blueshifted (blue), near-rest-frame velocity (green), or redshifted (red). Black lines point to specific dust features. For NIRSpec, the flux was integrated in a 2.5×2.5 arcsec^2 box centered on the ring to avoid noisy signal at the edges. In the MRS data, several lines ([Ne II], [Ne III]) originate from two distinct velocity ($v = 0$ and $v = 5000$ km s^{-1}) components. The [Ar II], [Ar III], [Ar V], [S III], and [S IV] emission lines mostly originate from blueshifted components, whereas the [O IV] line has multiple blue- and redshifted components. The H$_2$ lines trace the ISM along the same line of sight. In the NIRSpec data, the Brα line is the only line originating from the $v = 0$ km s^{-1} component, whereas the other lines appear to be emitted from a high-velocity ($v = 5000$ km s^{-1}) component.

Some of the Fe-bright clumps also emit in the NIRCam/F444W image, where the emission is likely dominated by nonthermal radiation and/or thermal emission from hot carbonaceous grains. The brightest emission filaments in the NIRCam/F444W image also correspond to the location of the dust emission visible in the MIRI images. However, most of the ring structures are less prominent in the NIRCam images (mostly absent in the F162M image and fainter in the F356W and F444W images), which confirms that the emission in the GM is largely dominated by dust emission across all MIRI filters. The green colors that outline the boundaries of several of these holes in the red-green-blue (RGB) image (see the first column of Figure 4) reveal that the dust temperatures in these rings are high compared to the rest of the GM emission and/or that the dust properties are different.

3.2. Spectral Decomposition and Analysis

In order to shed light on the nature of the GM and its position along the line of sight, we take a look at the kinematic information available in the MIRI MRS and NIRSpec data (see Figure 3) of the GM ring targeted in position P2 (see Figure 1).

We present an overview of the spectral line profiles in Figure 5 for several of the brightest lines in position P2, and we

discuss the fitting procedure to infer line fluxes and maps in Appendices A.1 and A.2. By performing this line fitting in each spaxel, we produced line intensity maps for the most prominent velocity components (see Figures 11 and 12). To briefly summarize our results, we find that the [O IV], [S IV], and [S III] lines have several velocity components tracing different SN ejecta filaments along the line of sight. In most cases, there is perfect agreement between the velocities of these various line emission components. This suggests that a contribution from the [Fe II] 25.99 μm line—which would show up as an extra line emission component shifted 0.1 μm with respect to the [O IV] line—is minimal. The absence of any other Fe lines makes a significant contribution from the [Fe II] 25.99 μm line unlikely. There is an interesting $v_{\rm rad} \sim 5000$ km s^{-1} filament that appears bright in [O IV], [Ne II], and [Ne III] but does not show any corresponding [S IV] or [S III] emission (see Figure 5). This $v_{\rm rad} \sim 5000$ km s^{-1} O-rich filament touches the base of the ring structure in position P2 (see Figure 11), and we will discuss the origin of its emission in scenario II of Section 4. Aside from this high-velocity component, there is [Ne II] and [Ne III] emission corresponding to a $v_{\rm rad} \sim 0$ km s^{-1} velocity component originating from the eastern part of the GM ring in this location (see Figures 5 and 12). Apart from the Ne
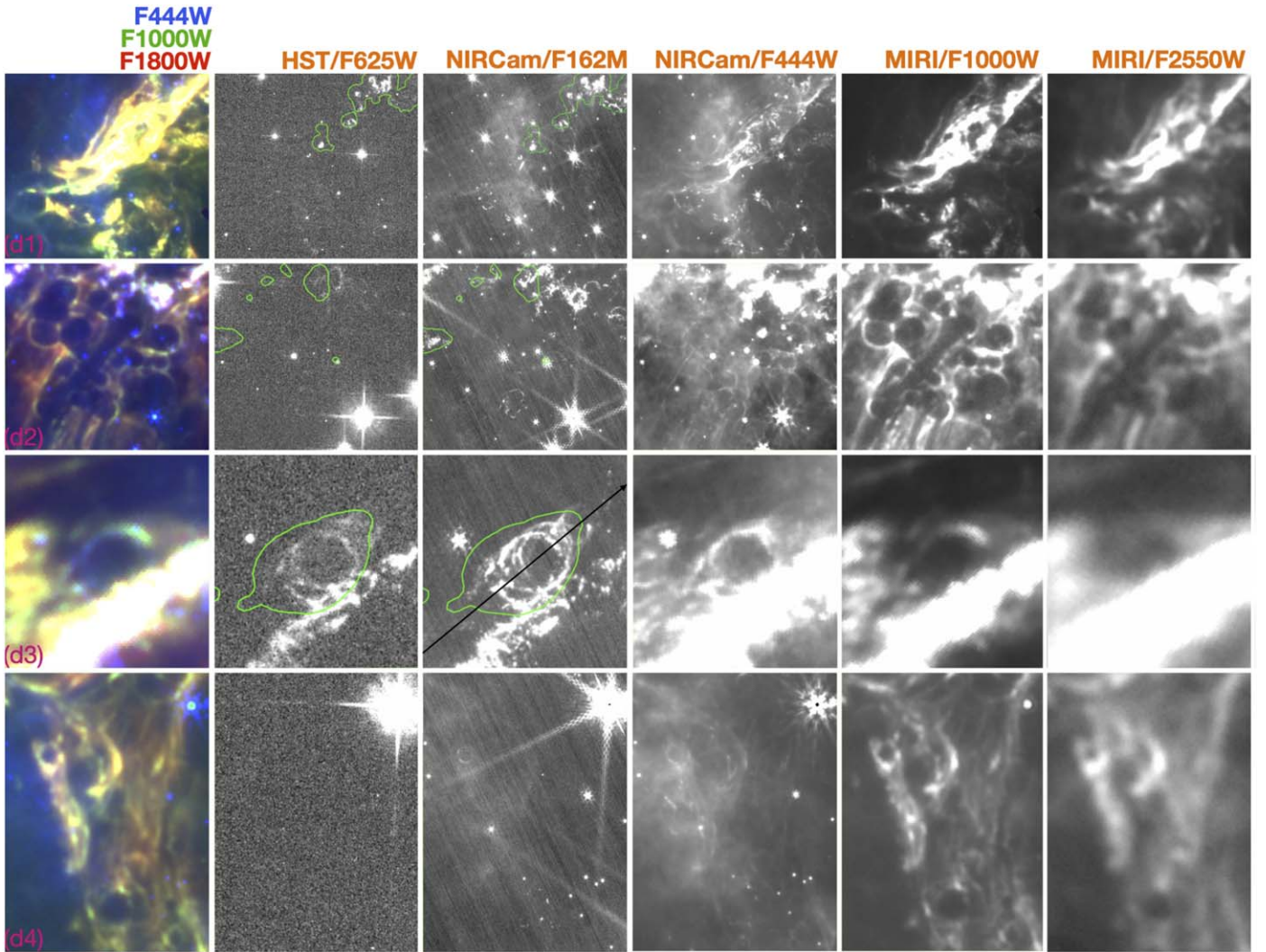
Figure 4. Multiwavelength view of the GM zoomed in on a few specific regions of interest (see the boxes in Figure 1 for their specific locations). The first column shows RGB images (blue: NIRCam/F444W; green: MIRI/F1000W; red: MIRI/F1800W) of each position, with the subsequent columns presenting the HST/F625W, NIRCam/F162M, NIRCam/F444W, MIRI/F1000W, and MIRI/F2550W images. The HST/F625W and NIRCam/F162M images have the contours of previously identified dense circumstellar clumps (QSFs) in deep [Fe II]+[Si I] (B.-C. Koo et al. 2018) imaging overlaid in green.

lines, faint emission near $v_{\rm rad} \sim 0$ km s^{-1} is also detected for the [Fe II] 17.94 μm and hydrogen Brα $n = 5 \rightarrow n = 4$ recombination lines. Table 1 presents an overview of the line fluxes that were inferred for this near-rest-frame velocity component.

Through convolution of the extracted spectra with and without line emission with the filter response curves, we are able to estimate the contribution of various lines to the MIRI broadband filters. We find that the average contribution of lines to the MIRI filters is limited, amounting to a few percent at most with the exception of the [O IV] 25.89 μm line, which significantly contributes to the JWST/MIRI F2550W filter ($\sim$16%). Assuming that the MIRI spectral data for this specific position in the GM are representative, we can conclude that the GM emission is dominated by dust continuum emission rather than line emission.

The complex kinematic structures along the line of sight reveal two velocity components (see Figure 5) with line emission resembling part of the dust continuum emission of the GM probed in the MIRI broadband filters. The dust emission in the ring structure on the east side is reflected in the [Ne II], [Ne III], [Fe II] 17.936 μm, and Brα line emission centered

around velocities of -50 to 0 km s^{-1} and also corresponds to the morphology of the [Fe II] 1.644 μm line emission in the NIRCam/F162M images (see Figure 7). On the other hand, the southern bright part of the ring is cospatial with the position of a bright O-rich ejecta filament with bright [O IV], [Ne II], and [Ne III] line emission with velocities around 5000 km s^{-1} (see Figure 11).

In the remainder of this section, we will discuss further observational evidence linked to the near-rest-frame velocity component that shows a spatial correlation with the eastern side of the one specific GM ring targeted with MRS observations that will help us to constrain the nature of the GM in Section 4.

3.2.1. Line Broadening

While the line flux maps of the [Ne II], [Ne III], [Fe II] 17.94 μm, and Brα lines nicely trace the eastern part of the GM ring in position P2 (first column of Figure 12) detected with MIRI in dust continuum emission, the radial velocities and velocity dispersions of these lines span quite a range of values with substantial positional variations (see
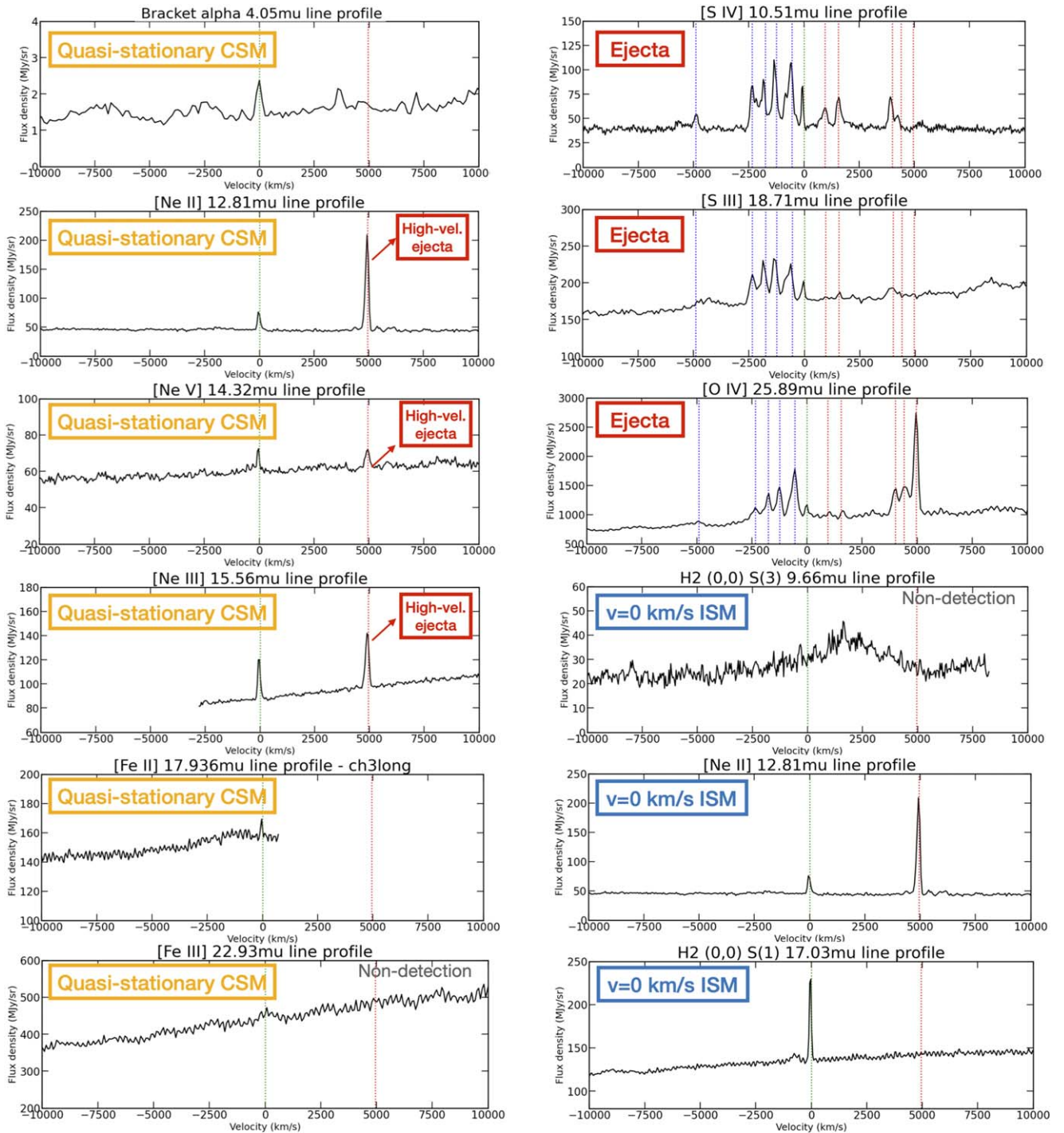
Figure 5. Line profiles for the brightest lines observed with NIRSpec and MIRI/MRS for the specific ring in the GM located in position P2 with the velocity on the *x*-axis, calculated relative to the rest-frame wavelength in vacuum for each of the transitions (see Table 1) and the line flux density (in units of MJy sr^{-1}) on the *y*-axis. The spectra were grouped depending on whether the emission originates from quasi-stationary (*v* near 0 km s^{-1}) CSM (yellow box), high-velocity ejecta material (red box), or interstellar material (blue box). In case of the neon lines, there is a contribution from quasi-stationary CSM near the rest-frame velocity and high-velocity ejecta material near 5000 km s^{-1}. The vertical dotted lines indicate different velocity components with blueshifts of −4900, −2350, −1750, −1250, and −550 km s^{-1} (in blue); a rest-frame velocity of 0 km s^{-1} (in green); and redshifts of +950, +1550, +4000, +4400, and +4950 km s^{-1} (in red) in the top three panels in the right column. The other panels have vertical lines overlaid to highlight velocity components with a rest-frame velocity of 0 km s^{-1} (in green) and a redshift of +4950 km s^{-1} (in red).

Figure 12, second and third columns). The broadening of the [Fe II] 17.94 μm and Brα line profiles appears to be solely driven by the instrumental resolution (i.e., ~100 and ~300 km s^{-1}, respectively). For both Ne lines, the brightest blob of emission toward the northeast shows the largest radial velocities and line widths, whereas the fainter region toward the

southeast does not show any significant broadening of the lines beyond what is expected from instrumental effects.

We now focus on the brightest blob of emission detected in the northeastern part of the ring in both Ne lines to study the extent of the line broadening. Correcting for the instrumental resolution—assumed to be ~90–100 km s^{-1} and ~120–130 km s^{-1} for the

[Ne II] and [Ne III] lines, respectively—we infer intrinsic FWHM line widths of $v_{\rm FWHM} \sim 150$ km s^{-1} and $v_{\rm FWHM} \sim 100$ km s^{-1} for [Ne II] and [Ne III], respectively. The significant broadening of these lines suggests the presence of shocked gas. However, while the northeastern part of the ring could be consistent with shocked gas, we cannot tell whether the gas in the remainder of this GM ring is shocked due to the limited spectral resolution. Later on, we will compare the observed line flux ratios with shock models to study whether the emission has been shock-ionized and excited or whether preionization of the unshocked material upstream can also contribute to the line emission (see Section 3.2.2)

We can now use these line widths to study the gas conditions. Assuming that nonthermal broadening is subdominant, we can estimate an upper limit on the gas temperature using

$$\text{FWHM [\AA]} \ = \ \lambda_0 \text{ [\AA]} \left(\frac{8 \, k_{\rm B} \, T \text{ [K] } \ln(2)}{m \, c^2} \right)^{1/2}, \qquad (1)$$

with the central wavelength λ_0, the Boltzmann constant $k_{\rm B}$, the speed of light c, and the mass m of the particles, in this case equal to $20 \times m_p$ for these Ne emission lines, with m_p the proton mass. We infer the velocity width from FWHM [km s^{-1}] $= c \times$ FWHM [\AA]$/\lambda_0$ [\AA], which suggests upper limits on the gas temperatures ranging from $T_{\rm gas} \sim 5 \times 10^6$ to 10^7 K. These gas temperatures would suggest shocked gas or postshock that has been radiatively cooled.

3.2.2. Photo- or Shock-ionized Material?

With several detected emission lines in the NIRSpec and MIRI MRS pointings coinciding with the specific GM ring structure in position P2, we attempt to constrain the physical conditions of the GM at that specific location. We focus on the near-rest-frame velocity component, since the line emission of a high-velocity component appears unrelated to the GM (see Section 4). We show several observed emission line ratios (see horizontal black lines) in Figure 6 and compare them with the estimates from the MAPPINGS III library of fully radiative shock models (M. G. Allen et al. 2008) at solar metallicity. The line ratios are depicted as a function of the modeled shock velocity. We overlay the model line ratios for MAPPINGS models with different preshock densities n of 10 (blue), 100 (green), and 1000 (red) cm^{-3}, and we consider models of shock-ionized emission (solid lines), preionization of unshocked material by the shock's radiation (dashed–dotted lines), and models that account for both effects (dotted lines).

Comparing the observed line ratios within the error bars (gray shaded regions) with the MAPPINGS models, the observations tend to be reproduced best by models with low shock velocities (100–300 km s^{-1}), which is consistent with the observed radial velocities of -50 to 0 km s^{-1}. For dedicated modeling efforts in future work, we will explore a finer grid of shock velocities, also extending below 100 km s^{-1}. The upper limits on [O IV]/[Ne II] and [Ne V]/[Ne II] line ratios and the observed [Ne III]/[Ne II] line ratio rule out pure photoionization models for high shock velocities ($v > 200$ km s^{-1}), whereas the observed [Ne II]/Brα and [Fe II] 17.94 μm/Brα line ratios suggest that shock ionization and excitation by high-velocity shocks ($v > 300$ km s^{-1}) is unlikely. At these low shock velocities, it is difficult to distinguish between pure shock or pure photoionization models or a combination of the two. While the observed [Ne II]/Brα and [Fe II] 17.94 μm/Brα line ratios would tend to favor pure shock ionization models, other

line ratios (e.g., [Ne III]/[Ne II] and [Fe II] 1.644 μm/[Fe II] 17.94 μm) are less conclusive.

We have already seen that some regions show significant line broadening that could be indicative of shocks, while others may be consistent with pure photoionizing radiation from shocks (see Section 3.2.1). Given that we are likely sampling a variety of conditions within this single GM ring, in addition to the potential effect of uncertain dust extinction corrections for some of the lines (e.g., [Fe II] 1.644 μm and Brα; see Appendix A.2), it is not surprising that models and observations are not in perfect agreement. For instance, the [Ne II] and [Ne III] line emission arises from two bright blobs within the ring with slightly different line emission ratios. The blob in the northeast has a below-average line ratio ([Ne III]/[Ne II] ~ 0.5) consistent with shock ionization with a potential contribution from preionization effects, which is consistent with the line broadening suggestive of shock excitation. The southeastern blob, on the other hand, is characterized by slightly higher line ratios, which could imply that photoionization plays a more prominent role.

3.2.3. Offsets between Line and Dust Emission

The rings are visible in dust continuum emission, and spectroscopic observations of a particular ring structure in position P2 (see Figures 7 and 12) also show that part of the ring structure emits in the [Ne II] 12.81 μm, [Ne III] 15.56 μm, Brα 4.05 μm, and [Fe II] 17.94 μm lines and potentially the [Fe II] 1.644 μm line in the NIRCam/F162M image. However, the line emission is consistently offset by $0''2-0''4$ from the dust emission toward the inner parts of the ring structure (see Figure 7). While belonging to the same structure, we argue that the offset between line and dust emission could be due to different densities, temperatures, and/or ionization conditions in the inner and outer parts of the rings. Alternatively, the offsets between line and dust emission could also result from the destruction of dust grains in the wake of the shock, resulting in the detection of line emission from Fe and other elements mostly in the inner ring regions. This last scenario seems to fit nicely with the warm IR colors of the rings in the GM (see the first column of Figure 4).

3.3. Blue- or Redshifted Material?

Both the resolved line modeling (see Figure 12) and the global extractions (see Table 1) suggest line velocities between -50 and 0 km s^{-1} for the Ne, Fe, and H line emission originating from the GM ring in position P2. But the large velocity dispersion (100–200 km s^{-1}; see Section 3.2.1) and the moderate velocity resolution (100–300 km s^{-1}) prevent us from drawing any firm conclusions on the position of this ring and the GM along the line of sight. Since the line emission detected in the MIRI MRS cubes for this specific ring location (P2) suggests that the GM is shocked, the measured radial velocities and internal velocity dispersion may have been affected by shock processing.

However, the significant blueshift (-2300 km s^{-1}) of the X-ray emission associated with several GM locations (J. Vink et al. 2024) firmly places the entire GM structure in front of Cas A. The difference in radial velocities measured at X-ray and mid-infrared wavelengths suggests that we are tracing distinct parts of the GM material at those wavelengths. The X-ray emission is tracing low-density material compared to IR.
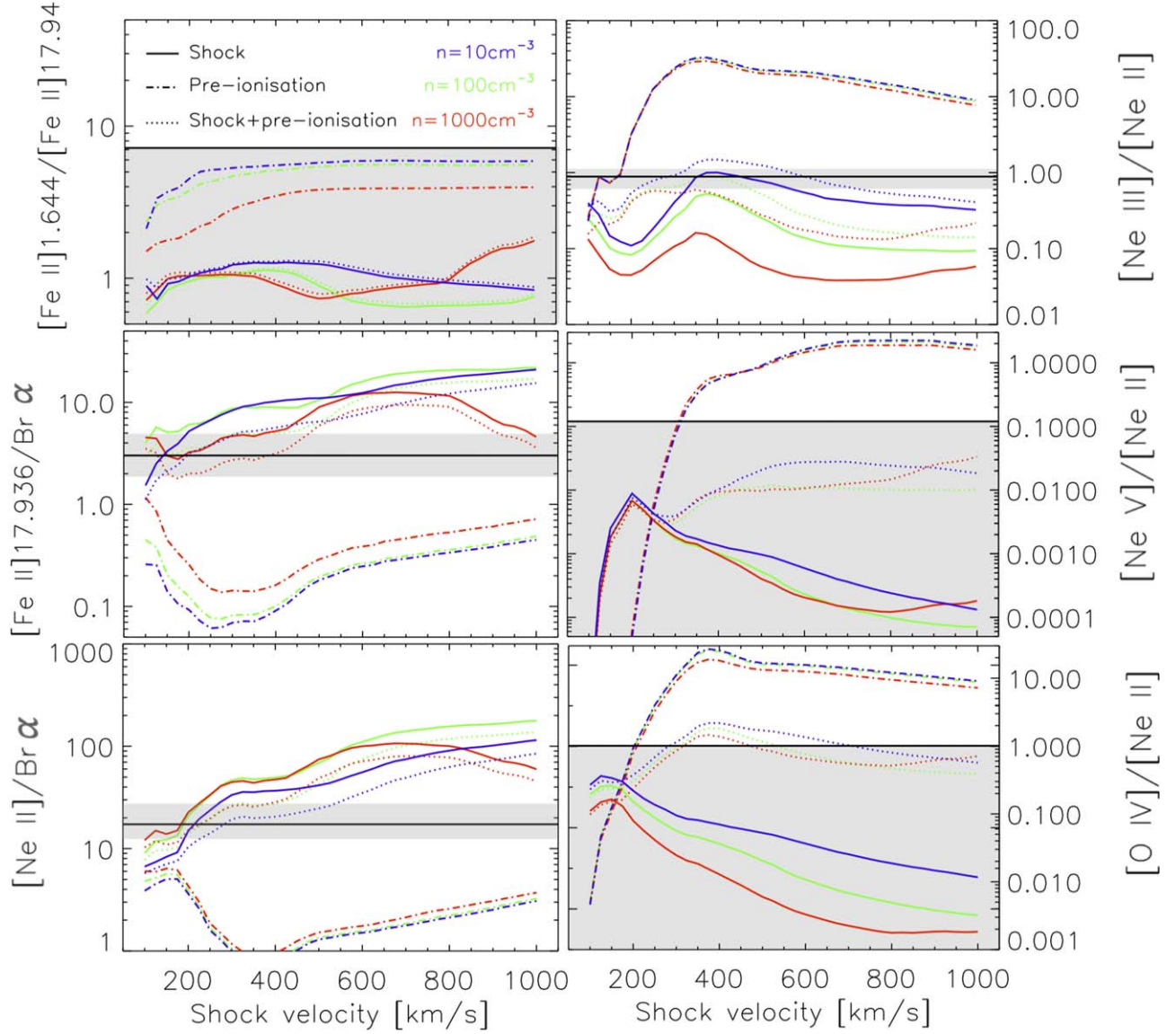
Figure 6. Comparison of the observed line ratios (gray shaded regions) with the library of radiative shock models from M. G. Allen et al. (2008) for models with different preshock densities n of 10 (blue), 100 (green), and 1000 (red) cm^{-3} and different ionization mechanisms: shock-ionized emission (solid lines), preionization of unshocked material by the shock's radiation (dashed–dotted lines), or both (dotted lines). The observations are consistent with low shock velocities (<200 km s^{-1}) but are unable to exactly pinpoint the ionization and excitation mechanism and the gas density.

The X-ray emission also originates mostly from a hot (>10^7 K) plasma (J. Vink et al. 2024), while the mid-infrared line emission could trace cooler (pre- or postshock) material in the GM. However, the significant line broadening in some parts of the GM ring (see Section 3.2.1) seems to suggest that temperature differences are rather small.

4. The Nature of the GM

In this section, we outline four different scenarios for the origin of the GM and discuss the probability of each scenario in light of the photometric and kinematic information available from the JWST observations and presented in Section 3. In brief, we inferred that low-velocity ($v_{rad} = -50$ to 0 km s^{-1}) Ne, Fe, and H line emission is cospatial with part of the GM ring in position P2 and reveals signatures (i.e., line broadening and shock ionization) of shocked gas. There is also a high-velocity ($v_{rad} = +5000$ km s^{-1}) filament that appears connected to the base of this GM ring structure.

In view of these findings, we outline four possible scenarios for creating the GM's circular structures visible in the NIRCam and MIRI images. Specifically, we considered scenario I, in which these circular structures are the result of the expansion of small Ni-rich ejecta; scenario II, in which they result from interactions of high-velocity ejecta filaments with dense circumstellar clumps on the rear side of Cas A; scenario IIIa, in which they are created through interactions with small, high-velocity ejecta "bullets" before the forward shock impact; and scenario IIIb, in which they form from interactions with ejecta fingers generated by hydrodynamic instabilities introduced at the contact discontinuity between the shocked layers of ejecta and CSM after the forward shock impact.

4.1. Scenario I: Ni Bubbles

Mapping out the unshocked ejecta, D. Milisavljevic & R. A. Fesen (2015) have shown that the remnant's interior has a bubble-like morphology that could be shaped through turbulent
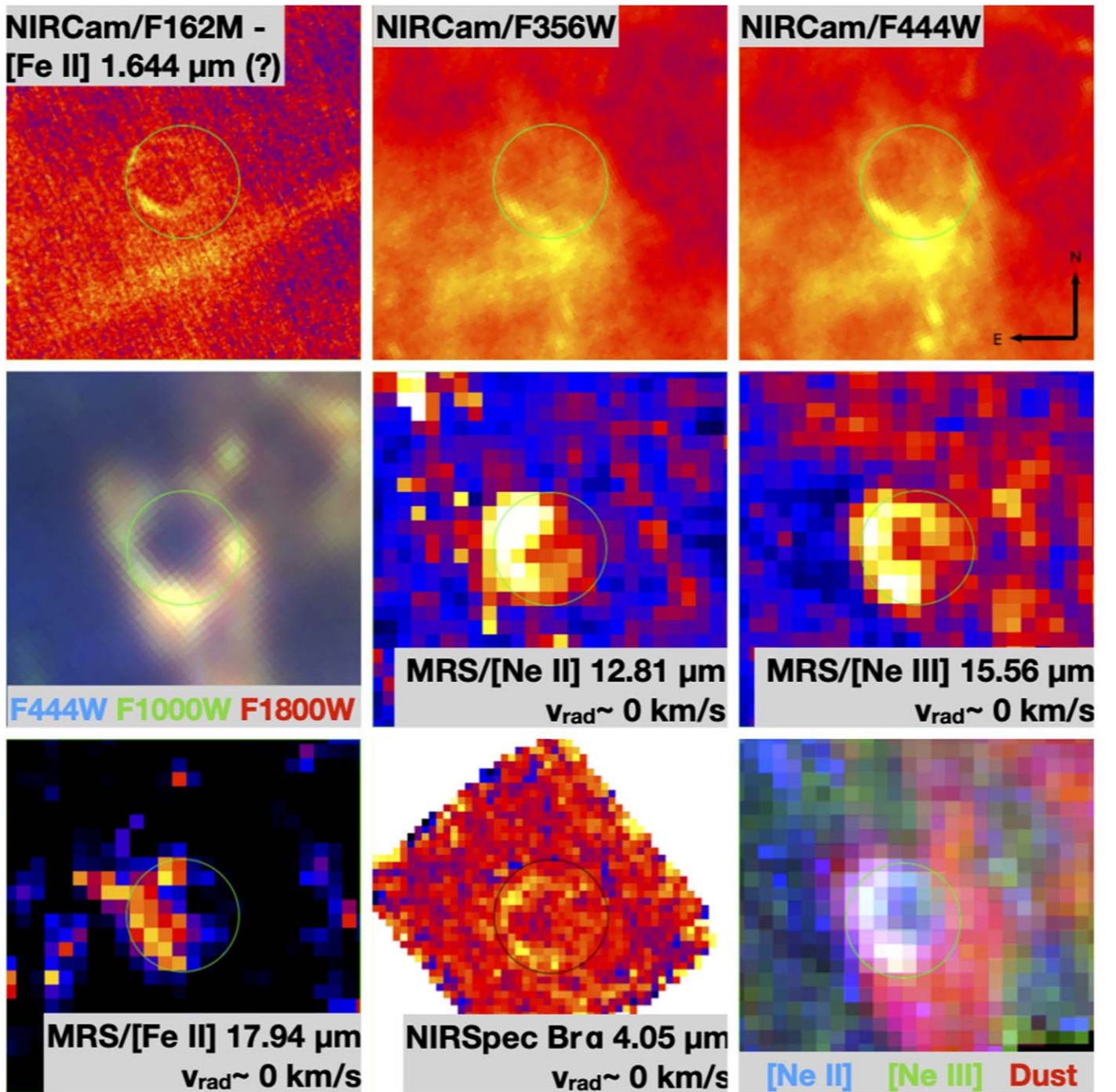
Figure 7. Multiwavelength view of the GM ring in position P2 (see Figure 1) showing the NIRCam F162M (PSF FWHM: $0\farcs055$), F356W (PSF FWHM: $0\farcs116$), and F444W (PSF FWHM: $0\farcs145$) images (top row); NIRCam+MIRI RGB image (F444W, F1000W, and F1800W with PSF FWHMs of $0\farcs145$, $0\farcs328$, and $0\farcs591$, respectively) and MRS line flux maps for the [Ne II] 12.81 μm (PSF FWHM: $\sim0\farcs529$) and [Ne III] 15.56 μm (PSF FWHM: $\sim0\farcs619$) lines (middle row); and MRS [Fe II] 17.94 μm (PSF FWHM: $\sim0\farcs698$) and NIRSpec Brα 4.05 μm (PSF FWHM: $\sim0\farcs15$) line flux maps for the near $v_{rad} = 0$ km s^{-1} velocity component and a multicolor RGB image comparing the dust with the line emission (bottom row). The images are at their native resolution; the FWHM of the PSF has been indicated in parentheses here for guidance. Each of the cutouts has the same $5'' \times 5''$ field of view. The green or black circle with a radius of $0\farcs8$ overlaid on the continuum and line emission maps serves to guide the eye when comparing dust continuum, synchrotron, and line emission in this region.

mixing processes that encouraged the development of outwardly expanding plumes of radioactive ^{56}Ni-rich ejecta material. The holes in the GM are reminiscent—although on much smaller scales—of these bubbles of radioactive ejecta that were inferred to have been ^{56}Ni-rich and that have shaped the multiple-ring structures and bubble-like morphology in

Cas A's ejecta (D. Milisavljevic & R. A. Fesen 2015). Hence, the GM could correspond to ejecta material in this case, and we would expect a substantial amount of the decay product, ^{56}Fe, in the interior of these cavities. The JWST data do not reveal any sign of Fe emission in the interior of the GM rings. Instead, Fe emission is only found in the GM rings in the form of [Fe II]

1.644 μm line emission traced in the NIRCam/F162M image and the [Fe II] 17.936 μm line emission detected in the GM ring covered with MIRI MRS.

In this ^{56}Ni bubble scenario, the GM would be located in the central regions of the remnant dominated by unshocked ejecta material. We have seen that the line broadening and shock excitation conditions of the mid-infrared lines imply that some of the GM material must originate from shocked gas, making this ^{56}Ni bubble scenario very low probability. The small size of the rings is also difficult to explain in this scenario, which would require a significantly slower expansion rate or recent expansion events in comparison to the bigger ^{56}Ni bubbles that have structured the inner ejecta of Cas A on much larger scales (D. Milisavljevic & R. A. Fesen 2015). Furthermore, the prominent mid-infrared dust emission is unlikely to originate from the unshocked ejecta since there are no radiative heating mechanisms that could heat the dust to such high temperatures ($T_{\mathrm{dust}} = 130$–300 K; I. De Looze et al. 2024, in preparation).

4.2. Scenario II: Interaction between High-velocity Ejecta Filaments and Dense Circumstellar Knots

In this scenario, we discuss two possible interpretations under the assumption that the observed connection between the high-velocity ejecta filament and the GM ring in position P2 is not a mere coincidence due to projection effects but rather results from a physical link implying an interaction between a high-velocity ejecta filament and the GM material.

First, we postulate that the GM could result from interactions between high-velocity ejecta filaments and dense CSM knots. Instead of holes, the ring structures would correspond to dense CSM clumps that are currently impacted by Cas A's high-velocity ($\sim$5000 km s^{-1}) O-, S-, and Ar-rich ejecta filaments (see Figure 11). Upon impact, the high-velocity material continues its path most easily around the dense CSM knots. Zooming out to have a wide-angle view, we can see that there is indeed a large-scale, >1 pc in size, ejecta filament that touches upon the GM ring targeted in MIRI MRS observations (see Figure 2). The increased intensity of the [O IV] 25.89 μm line around 5000 km s^{-1} suggests that an interaction is taking place at that specific position corresponding with the bottom part of this ring structure (see Figure 11). If we assume that this high-velocity ejecta filament is hitting a high-density circumstellar clump, these clumps would need to be optically thick beyond 30 μm and/or the dust would need to be very cold to prevent emission in the JWST MIRI filters. However, the absence of any large-scale filaments coinciding with other rings in the GM makes this an improbable scenario. It is furthermore unclear how the interaction of a high-velocity ejecta filament could create ring structures as observed in the GM—it would be more likely for an arc-like structure to form in this case.

Assuming ballistic motion of this high-velocity ($v = 5000$ km s^{-1}) oxygen-rich ejecta filament, we estimate that an impact occurs at a distance of about $\gtrsim$1.79 pc from the explosion center for an explosion that occurred 350 yr ago. This position corresponds with the average position of the reverse shock estimated in the plane of the sky (J. Vink et al. 2022). Assuming that the evolution of the forward and reverse shocks has progressed in a similar way on the rear side of the remnant, this high-velocity ejecta filament could be traversing the reverse shock. In this case, the GM could correspond to a sheet of high-velocity ejecta material that is currently encountering the reverse shock. The holes would be created

by dense CSM knots that must have survived the blast wave and now happen to lie in the vicinity of the reverse shock.

The interaction between the ejecta material and the dense CSM knots would produce low-velocity line emission on the surface of the CSM clumps, in which case the observed rings would correspond to the limb-brightened surfaces of the CSM clumps. Since we only observe low-velocity ($v_{\mathrm{rad}} = -50$ to 0 km s^{-1}) line emission cospatial with the GM ring targeted in MRS observations, and no velocity information linked to the whole of the GM structure is available, we cannot rule out that the GM dust-emitting material is moving at high velocities ($\sim$5000 km s^{-1}). However, we consider it unlikely that the GM would correspond to high-velocity ejecta material that is currently hit by the reverse shock. Shock ionization upon traversing the reverse shock makes ejecta knots emit brightly in mid-infrared lines (T. DeLaney et al. 2010; D. Docenko & R. A. Sunyaev 2010) along with bright dust emission (J. Rho et al. 2008; R. G. Arendt et al. 2014), whereas the GM appears to be mostly dominated by dust continuum emission. The absence of any O, S, or Ar lines in the GM ring within position P2 suggests that line emission is negligible, at least in this region. We therefore consider this scenario to be unlikely.

Instead, we argue that the interaction of the high-velocity ejecta filament with the reverse shock is unrelated to the GM and happens coincidentally on the same line of sight. If we compare the emission of this specific GM ring to similar ring structures observed with broadband JWST/MIRI filters in the GM, it also becomes evident that the emission in the (partial) ring surrounding the empty hole is much more pronounced (see Figure 7), in particular at the bottom, which suggests that the nature of this particular ring may be different. Thus, we argue that part of the ring structure toward the base of the ring in this MIRI MRS pointing is contaminated by high-velocity ejecta impacting the reverse shock on the rear side of the remnant.

4.3. Scenario III: Forward-shocked Circumstellar Dust with Holes Created by Ejecta Interactions

In our preferred scenario, we argue that the dust-emitting GM corresponds to CSM that has been impacted by the forward shock, and the circular structures are created by interactions with ejecta material. Several lines of evidence support this scenario. The small-scale structure of the GM resembles the circumstellar dust seen toward the north and southwest of Cas A. In comparison, shocked ejecta filaments are composed of small knots and ejecta shrapnel that formed in the aftermath of the explosion, which are not visible in the GM. In addition, the similar shape of the mid-infrared dust emission spectrum of the GM and the CSM seen in projection toward the northeast and south of Cas A (I. De Looze et al. 2024, in preparation) suggests that the dust composition is similar, hinting at the same chemical makeup of the material and similar pathways that have led to dust formation.

There is also a correlation between the X-ray emission and the dust emission in the GM (J. Vink et al. 2024), which supports the shock interaction scenario. An X-ray analysis of the GM (J. Vink et al. 2024) further corroborates this conclusion. X-ray spectral extractions across different regions of the GM show consistently blueshifted emission corresponding to shock velocities of -3500 km s^{-1}. These shock velocities are representative of the forward shock speeds measured for Cas A in the plane of the sky (5000–7000 km s^{-1}; J. Vink et al. 2022), although somewhat on the low side, and

reveal that the CSM in the GM is likely interacting with the forward shock on the nearside of the SNR. The presence of dense CSM in front of Cas A would have caused the forward shock to slow down, which is consistent with the measured slow forward shock speeds.

Furthermore, we find a match between the position of the GM and the location of a handful of dense circumstellar clumps, the so-called QSFs. In Figure 8, we overlaid the positions of the more than 50 QSFs identified from optical and NIR data (B.-C. Koo et al. 2018) on a multicolor JWST/MIRI image (right panel). A high-resolution comparison is shown in Figure 4 (see the contours in the second and third columns) for some specific regions. These figures reveal that some of the QSF positions align well with the GM's dust emission. The broadening (100–200 km s^{-1}) of the observed line emission in the GM ring targeted with MIRI MRS is furthermore consistent with the significant broadening ($\sim$200 km s^{-1}) observed for shocked QSFs around Cas A (B.-C. Koo et al. 2020), which is in sharp contrast with the expected line width of unshocked CSM ($\sim$8 km s^{-1}) and suggests that some GM rings host dense shocked CSM.

However, it is important to note that there is not a perfect one-to-one correlation between the QSFs and the rings detected in the GM. We will return to a discussion on the origin and connection to the various CSM components in more detail in Section 5.

Finally, an important clue comes from the line emission that is associated with the dust-emitting ring structure. We observe the emission of Ne- and Fe-rich material at near-rest-frame velocities (-50 to 0 km s^{-1}) tracing the eastern side of the ring structure (see Figure 12). In the NIRSpec data, we also observe hydrogen Brα line emission near 4.05 μm, which suggests that the material is enriched with hydrogen. This scenario is further corroborated by the detection of Hα emission coinciding with several dense Fe-rich clumps in the GM (see Figure 4). Given that Cas A resulted from a Type IIb explosion, we expect little hydrogen to be present in the ejecta. Hence, the small radial velocities and the detection of hydrogen, neon, and iron emission lines perfectly fit the picture of CSM ejected 3×10^4–10^5 yr before the SN explosion (calculated for wind velocities ranging from 30 to 100 km s^{-1}).

While we are confident that the GM corresponds to CSM, the exact details of the mechanism capable of creating the circular rings and holes are still missing. We outline two possible scenarios (IIIa and IIIb), which both involve CSM interactions with especially high-velocity small ejecta knots to create the observed circular rings.

4.3.1. Scenario IIIa: Fast-moving Ejecta Knots Pierce Holes before Forward Shock Impact

Here we postulate that small, fast-moving ejecta bullets have pierced holes in a thin sheet of CSM, which would create a shock wave moving radially through the CSM layer such that it creates a hole that becomes larger over time (in the absence of any external pressure source, such as a new shock impact). In this view, the creation of these holes would require ejecta knots that have been accelerated to very high velocities in the aftermath of the explosion, and, in fact, such high-velocity ejecta knots have been identified around Cas A (R. A. Fesen 2001; R. A. Fesen et al. 2006, 2011;

M. C. Hammell & R. A. Fesen 2008; R. A. Fesen & D. Milisavljevic 2016). While S-rich and O-rich FMKs with velocities ranging between 7000 and 15,000 km s^{-1} have been identified in Cas A's northeast and southwest jet regions, several dozen N-rich FMKs have been detected out beyond the remnant's bright ejecta ring and X-ray-detected forward shock front with nearly isotropic ejection velocities of 8000–10,500 km s^{-1} (R. A. Fesen 2001; R. A. Fesen et al. 2006). The detection of these high-velocity knots tends to be limited to the ones moving nearly in the plane of the sky (with a maximum offset of 30°), which maximizes the ability to detect the shock excitation and ionization of these ejecta knots when they encounter circum- or interstellar material (R. A. Fesen 2001; R. A. Fesen et al. 2011).

While the distribution of S-rich and O-rich FMKs tends to be clustered in the northeast and southwest jets of Cas A, the observed distribution of the near-tangential N-rich FMKs covers a much wider range of position angles, which suggests that these N-rich knots were ejected isotropically, which is also reflected in their nearly uniform space velocities ($\approx$8000–10,500 km s^{-1}). This makes these high-velocity N-rich knots perfect candidates to pierce through the circumstellar shell, clearing the material inside the shell and creating mini-shock waves traveling perpendicular to the direction of the ejecta knot's motion.

The average shock velocities $v_{\mathrm{shock}} = -3500$ km s^{-1}—as inferred from X-ray spectra of the GM (J. Vink et al. 2024)—indicate that the expansion has been slower on the nearside of the remnant, similar to the slow shock velocities measured toward the south (position angle of 190°; J. Vink et al. 2022). However, it is unclear whether shock velocities have been consistently lower compared to the other directions. We conservatively estimate that the forward shock position along the line of sight is similar to the location of the forward shock measured in the plane of the sky (2.8 pc; J. Vink et al. 2022). N-rich FMKs would have impacted a shell of CSM positioned at a distance of 2.8 pc from the explosion center about $\sim$274–304 yr postexplosion. That would mean that the impact already occurred around $\sim$45–75 yr ago, and that the material in the circular structures has been expanding since.

These outer N-rich ejecta knots appear quite small on HST images but are in reality hundreds of au in size. The average angular size of these FMKs is 0″.1 (R. A. Fesen & D. Milisavljevic 2016), but there are several HST-resolved N knots with sizes as large as 0″.3 (i.e., around 1000 au). The apparent clustering of GM holes in certain areas is also consistent with the grouping of N-rich ejecta knots around the periphery of Cas A (R. A. Fesen 2001; M. C. Hammell & R. A. Fesen 2008). Combining their size with their fairly high densities ($n_e \sim 2$–10×10^3 cm^{-3}; R. A. Fesen 2001), these hypersonic ejecta projectiles should be capable of making large expanding impact rings in the GM. Compared to the observed size of the ring, we estimate that average shock velocities of $\gtrsim$200 km s^{-1} are required to expand the puncture to the size of the present-day circular structures.

Alternatively, it is possible that compression waves originating from the displacement of the CSM lead to the increase of density and hence emission measure at the border of the holes. Unless the FMKs arrived at exactly the same time, the roughly similar sizes of the rings in the GM suggest that the
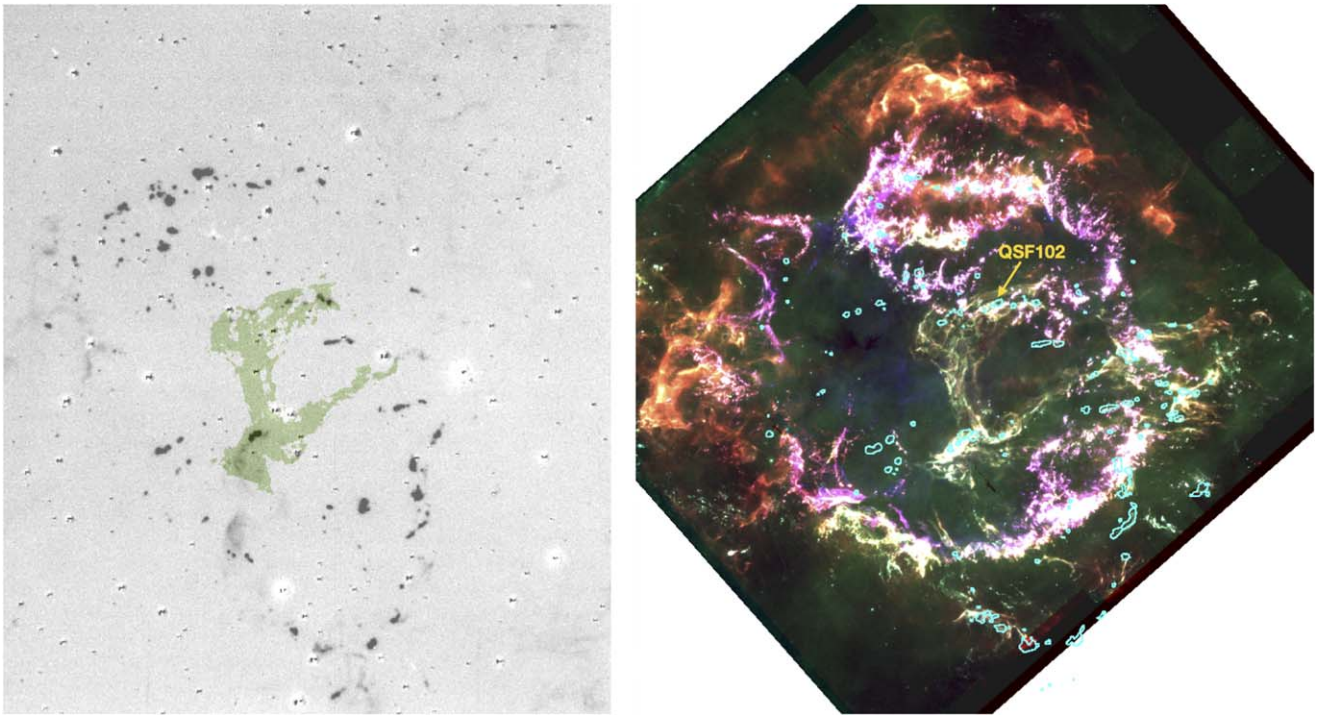
Figure 8. Left: the locations of dense CSM clumps, often called QSFs, as traced by Hα emission. The figure was adapted from R. A. Fesen (2001) to show a green outline of the location of the GM, which nicely fits in the middle of the formerly identified dense CSM knots. Right: multicolor MIRI image (blue: F1000W, green: F1130W, red: F2550W) with contours indicating the locations of these dense QSFs as identified by B.-C. Koo et al. (2018).

ring size is where the expansion stalls given the transverse momentum deposited in the collision. In this case, the ring would be the result of pileup of material rather than shock heating.

The observed line emission interior to the dust-emitting part of the rings and the predominantly warm dust emission in the GM rings (compared to the remainder of the GM) would suggest that shock heating and dust destruction by shock waves are relevant, favoring the shock-wave scenario. Unfortunately, we are not able to further test these two scenarios by estimating the velocities of the shock waves that created the circular holes since the MRS spectra are dominated by radial gas motions and hardly trace the tangential motion of these shock or compression waves in the plane of the sky. Furthermore, the material in these rings would cease to expand upon forward shock impact, and we can expect these rings to gradually start shrinking.

The formation of complete or partial ring structures will depend on both the density of the CSM and its density fluctuations. The absence of full ring structures can likely be attributed to (i) intrinsic density variations in circumstellar shells, (ii) an impact angle of the ejecta bullet that is not perpendicular to the CSM layer, or (iii) multiple impacts by a tight cluster of fast-moving ejecta knots that have diluted the densities in these regions. The GM location that is pockmarked with a dozen holes (see position (d2) in Figure 4) is likely an example of a complex region where several fast-moving ejecta knots impacted the CSM and where the density is lower (either intrinsically or due to the earlier impacts), creating these partial ring structures.

The multiple-ring structure (see position (d3) in Figure 4) can also be interpreted in view of this scenario. The negligible radial velocity of the QSF associated with this structure ($v_r = 6 \pm 22$ km s^{-1} for QSF 102; B.-C. Koo et al. 2018; see also the right panel of Figure 8) and the substantial tangential

velocity component (1300 km s^{-1}) inferred from a proper-motion study ($\sim 0.''08$,[35] position angle of $-60°$; B.-C. Koo et al. 2018) would imply that the CSM in this region is tilted with respect to the line of sight. In this case, the multiple-ring structure could reflect different layers of CSM that are punctured by the same fast-moving ejecta knot. The multiple-ring structure is only clearly visible in the NIRCam/F162M image, likely originating from [Fe II] 1.644 μm line emission. The lack of dust continuum emission for most of the partial rings in this region may suggest that dust has been destroyed (which would explain the presence of Fe in the gas phase). The black arrow overlaid on the NIRCam/F162M image of position (d3) in Figure 4 outlines the potential trajectory from a fast-moving ejecta knot tracing back to the center of the explosion.

The good agreement between the alignment of the rings in this position and the trajectory of ballistically moving ejecta knots supports the scenario of ejecta bullets impacting on CSM shells. We note that R. Braun et al. (1987) already witnessed bow shocks in radio maps resulting from ejecta clumps impacting on decelerated shell material. While these bow shocks result from large, more diffuse condensations of ejecta material, they postulate that small, high-density fragments would have little dynamical impact on the shell and would leave expanding rings of compressed material.

Since little mid-infrared dust continuum emission appears to be arising from inside the GM rings, this would suggest that only a thin layer of CSM is emitting. If an ejecta knot plows through a layer of CSM at a given angle with respect to the line

---

[35] The proper motion is measured from the positional shift in the intensity-weighted centers of the knot in the 2008 and 2013 images. The largest source of uncertainty is associated with the change in morphology due to intensity variations within the knots and is difficult to quantify.
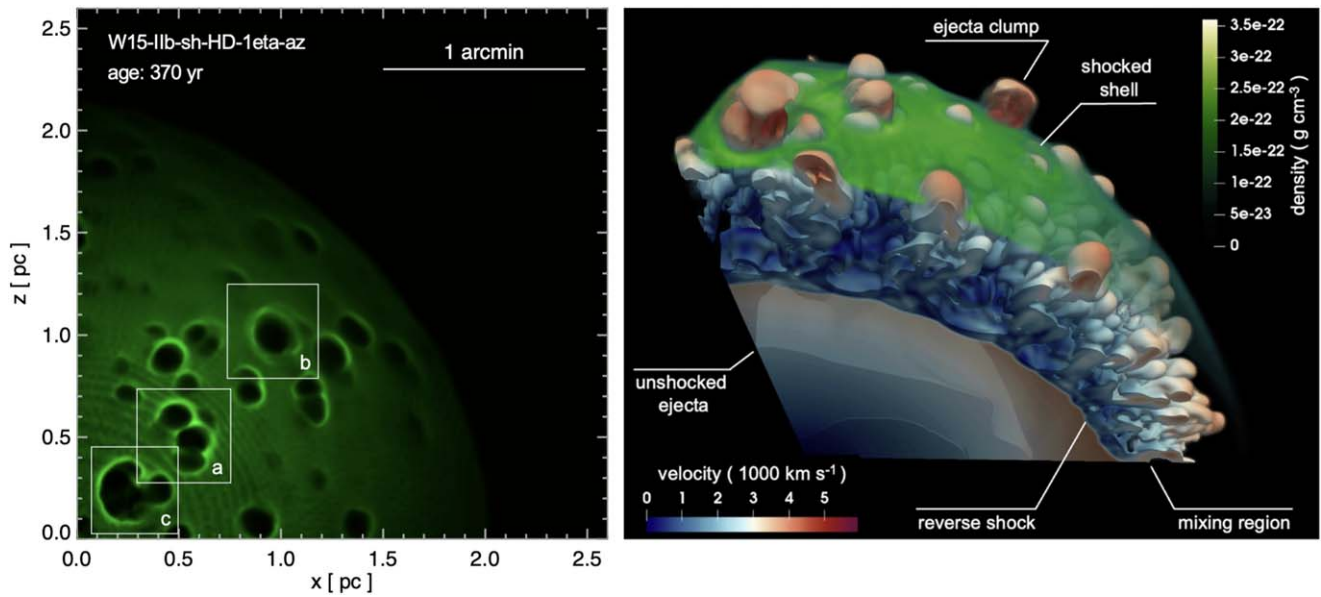
Figure 9. Structure of a circumstellar shell after interaction with the remnant at the age of Cas A, as derived from a three-dimensional hydrodynamic simulation (run W15-IIb-sh-HD-1eta-az in S. Orlando et al. 2022). Left panel: three-dimensional volume rendering of the particle density of the shocked shell material (density integrated along the line of sight). Only the upper right quadrant of the numerical domain is shown. The three white square regions mark holes, which are shown enlarged in Figure 10, in comparison with similar structures observed with JWST. Right panel: detail of the structure of the ejecta and their interaction with the shell at the age of Cas A. The semi-opaque irregular isosurfaces correspond to a value of ejecta density, which is at 1% of the peak density; their colors represent the radial velocity in units of 1000 km s^{-1} on the isosurface (the color coding is defined in the bottom left corner of the panel). The three-dimensional volume rendering in green describes the particle density of the shocked shell material (see color bar on the right of the panel).

of sight, we would expect part of the ring to be filled with emission from a CSM layer that is not parallel with the plane of the sky. The absence of such filled rings suggests that the CSM layer must be intrinsically thin ($<0\rlap{.}''32$) where we used the FWHM of the highest-resolution MIRI/F1000W image in which the rings are unresolved. This would suggest that the dense CSM has been lost during a brief mass-loss episode that lasted <300 yr if we assume a typical mass-loss velocity for RSGs ($10\,\mathrm{km\,s^{-1}}$). The radial velocities of QSFs instead suggest that the material has been lost during a faster ($100\,\mathrm{km\,s^{-1}}$) mass-loss episode, which would restrict the mass-loss duration to <30 yr. These values are not unrealistic given the mass-loss variability observed in various RSGs (e.g., R. M. Humphreys & T. J. Jones 2022).

Alternatively, the thickness of the observed GM rings could be representative of the dust destruction length scale. This dust destruction length scale would depend on the average shock speed, the gas density, and the grain size of the dust. The observations would require the dust to be destroyed within 30 yr time after shock passage if we assume that the material in the ring is flowing at speeds of $100\,\mathrm{km\,s^{-1}}$. To destroy the small grains ($<0.01\,\mu\mathrm{m}$) that preferentially emit at these mid-infrared wavelengths, we would require dust grains to be exposed to the hot X-ray-emitting gas ($>10^6$ K), where these small grains can be efficiently sputtered. Such dust destruction timescales for small grains are not unrealistic (e.g., F. Kirchschlager et al. 2019, 2023). Using the formula from C.-Y. Hu et al. (2019) for the sputtering timescale,

$$t_{\mathrm{sput}} \approx 0.33\,\mathrm{Myr}\left(\frac{a}{\mu\mathrm{m}}\right)\left(\frac{n_\mathrm{H}}{\mathrm{cm^{-3}}}\right)^{-1}\left(\frac{Y}{10^{-6}\,\mu\mathrm{m\,yr^{-1}\,cm^3}}\right),\tag{2}$$

we estimate an average destruction timescale of $\sim$33 yr for a 5 nm grain, a density of $50\,\mathrm{cm^{-3}}$ (based on the estimates of the X-ray-emitting gas from J. Vink et al. 2024), and a total sputtering yield of $Y_{\mathrm{tot}} = 10^{-6}\,\mu\mathrm{m\,yr^{-1}\,cm^3}$. In this scenario, we pick up emission of dust grains that are rapidly being destroyed (on timescales of several tens of years) in the GM rings after the shock impact.

4.3.2. Scenario IIIb: Hydrodynamic Instabilities Create Protruding Ejecta Fingers after Forward Shock Impact

Rather than fast-moving ejecta bullets creating holes in the GM prior to the forward shock impact, it is possible that the forward shock impact triggers hydrodynamic instabilities (Rayleigh–Taylor, Richtmyer–Meshkov, and Kelvin–Helmholtz shear instability) at the contact discontinuity that create fingers and clumps of ejecta extending beyond the contact discontinuity to the shocked dense shell of CSM. These fingers protrude into the shocked shell material, which produces holes in the shell similar to the ones observed in our JWST observations.

Three-dimensional hydrodynamic simulations (S. Orlando et al. 2022) were performed prior to the discovery of these holes in the circumstellar GM structure with JWST and were designed to model Cas A's remnant evolution from the collapse of the stellar core to the actual age of Cas A (see also A. Wongwathanarat et al. 2017; S. Orlando et al. 2021), including the interaction of the SN blast wave with a massive circumstellar shell.

According to these simulations, the asymmetric circumstellar mass loss resulted from a massive eruption in the progenitor star roughly 10,000–100,000 yr prior to the explosion, and the remnant first encountered the shell roughly 200 yr after the explosion. According to the model, the densest portion of the shell is located on the blueshifted nearside of the remnant, consistent with the position inferred for the GM. The ensuing shock accelerated the circumstellar shell material to velocities
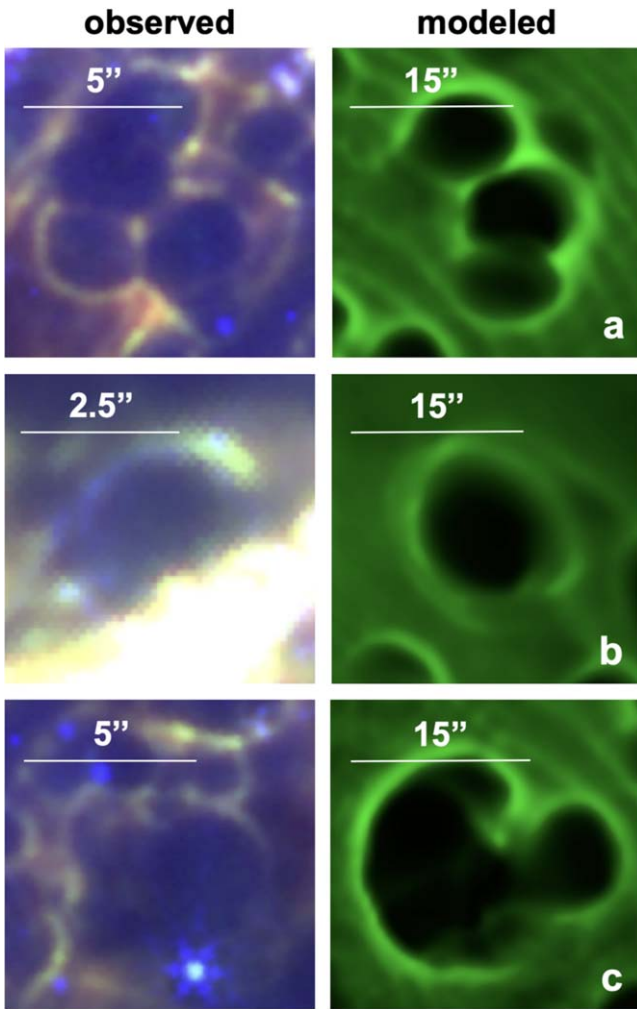
Figure 10. A comparison between holes and rings observed with JWST (left panels) and analogous structures predicted by hydrodynamic simulations (right panels; S. Orlando et al. 2022) and identified in the white square regions in Figure 9.

of around $3000 \, \text{km s}^{-1}$, in agreement with the values inferred from the analysis of X-ray observations (J. Vink et al. 2024). Soon after it was shocked, the shell started to interact with filamentary structures and clumps of ejecta, rapidly expanding from the contact discontinuity toward the forward shock. These protruding fingers and clumps penetrated the shocked shell material, forming circular holes within its structure. Figure 9 shows a detailed view of the shocked shell's structure (left panel) at the age of Cas A, derived from model W15-IIb-sh-HD-1eta-az in S. Orlando et al. (2022), along with the mechanism driving the formation of the holes (right panel).

The material within the voids is displaced by the advancing fingers and clumps, gradually accumulating along the hole's periphery, resulting in higher density in those regions (see left panel of Figure 9). The cavities and rings formed in this way display shapes remarkably similar to those witnessed with JWST (see the enlarged regions in Figure 10). More specifically, we observe that the model can naturally reproduce, in addition to full regular ring structures, regions pockmarked with several holes partially overlapping each other (upper panels in Figure 10), as observed in region (d2) in Figure 4; multiple-ring structures (middle panels in Figure 10), as observed in region (d3) in Figure 4; and partial rings (lower

panels in Figure 10), as observed, for instance, in Figure 7. These features originate from ejecta fingers and clumps that extend from the contact discontinuity and interact with the shocked shell, even though the modeled shell is not characterized by small-scale density fluctuations.

Model simulations also reveal that, on average, the radial velocity of the ejecta structures that interacted with the shell is lower than in regions where such interaction did not occur, due to the passage of the reflected shock from the shell that decelerated the ejecta clumps. The simulated holes have diameter sizes in the range of $\approx 3''-18''$ ($\sim 0.05-0.3$ pc), significantly larger than those observed in the GM (see Figure 10). This difference in size primarily stems from the limited spatial resolution of current simulations, which impedes an accurate description of the small-scale structure of the ejecta. To accurately capture the size of the observed holes, dedicated simulations with higher spatial resolution will be necessary (S. Orlando et al. 2024, in preparation).

With the present data, we are unable to select a preferred scenario. One of the main differences between scenarios IIIa and IIIb is the creation mechanism for the GM rings and the associated timescale. If we assume that the holes were created prior to interaction with the SN blast wave by fast-moving ejecta bullets that move ahead of the forward shock (scenario IIIa), this would create a time gap of $\sim 15-45$ yr between the creation of the holes and the forward shock impacting on this CSM. While there is evidence for the existence of such FMKs, it is unclear whether the forward shock interaction would be able to maintain the morphology of the circular rings. There is evidence that the GM has been shocked already for at least 30 yr, which would require the circular rings to have incredibly high densities in order to avoid distortion of these circular structures upon shock impact.

This problem could be remedied if we are probing a thin layer of recently shocked material in which small grains are not yet completely destroyed. On the other hand, we would expect to observe ring structures that are partially filled when observing fingers of ejecta clumps penetrating through a shocked circumstellar layer inclined with respect to the line of sight. In the simulations, the shell has a thickness of ~ 0.02 pc, whereas the observations would constrain the shell thickness to be 10 times smaller. It is possible that the destruction timescale also has an impact here on what we are observing. It is furthermore unclear whether the evolution of the hydrodynamical instabilities—resulting in the creation of GM-like ring structures—could have been influenced by the three-dimensional nature of the progenitor and its three-dimensional mass loss instead of the assumed one-dimensional progenitor model (S. E. Woosley & T. A. Weaver 1995), whose core collapse was evolved through several simulation stages (A. Wongwathanarat et al. 2017) that finally led to the input model of S. Orlando et al. (2021, 2022). Future work will need to study the impact of some simplifications in the progenitor and SN explosion models (e.g., nonturbulent CSM/ISM structure and smooth shells) on the late-time interaction with the reverse shock and CSM and the subsequent formation of ringlike structures similar to the observations with JWST in the GM. Currently, ongoing efforts (S. Orlando et al. 2024, in preparation) are dedicated to studying the combined effects of efficient radiative cooling (which makes ejecta fingers and clumps thinner and denser) and the magnetic field's

confinement of ejecta structures (which enhances radiative losses) on the rings' shapes and sizes.

5. Discussion

5.1. Cas A's Mass-loss History

In this paper and a companion paper (J. Vink et al. 2024), we argue that the newly detected GM structure pockmarked with holes corresponds to circumstellar dusty material that was lost by the progenitor star about 3×10^4–10^5 yr prior to explosion. A valid question to ask ourselves is how the GM is related to other mass-loss phases.

Comparison of dust SEDs (I. De Looze et al. 2024, in preparation) and X-ray spectra (J. Vink et al. 2024) suggests that the GM closely resembles the properties of the southern arc of CSM that is currently impacted by the SN blast wave and that was already identified from early optical observations (S. van den Bergh & K. W. Kamper 1983; S. van den Bergh & K. Kamper 1985; S. S. Lawrence et al. 1995). A significant number of QSFs are located in the southern circumstellar arc or the GM, which may suggest that QSFs are linked to the same mass-loss phase that ejected this CSM. In addition, several QSFs are located along the shocked main ejecta shell in the north or scattered randomly within the main ejecta shell. We suggest that these QSFs may be connected to CSM that is interacting with high-velocity ejecta knots, which are prominently seen in the main ejecta shell in the north (R. A. Fesen et al. 2011).

In Figure 8 (left panel), we show that the GM's location fits in well within the elongated shell-like structure of dense shocked CSM knots discerned through their Hα emission (R. A. Fesen 2001). This picture gives high credibility to a scenario where the GM and QSFs were ejected by the Cas A progenitor star during the same mass-loss episode. This suggests that the mass loss experienced by the progenitor star resulted in one-sided mass loss on the nearside of the Cas A system. In this view, QSFs most likely represent small clumps of especially high densities in the remnant's circumstellar medium.

While the GM appears to resemble the properties of the circumstellar dust in the southern arc, its green color clearly distinguishes the GM from the yellow, orange, and red circumstellar clouds located in the north, east, and west of Cas A. In a follow-up work (I. De Looze et al. 2024, in preparation), we will discuss how the grain composition and size varies for circumstellar dust formed from material lost during distinct mass-loss episodes. The diffuse red circumstellar clouds in the north, east, and west of Cas A also stand out for not hosting any QSFs (B.-C. Koo et al. 2018). A close examination of the NIRCam/F162M image confirms that—apart from one region that shows evidence for interaction with ejecta knots—there is no trace of Fe emission in these red circumstellar clouds (B.-C. Koo et al. 2024, in preparation).

While the bulk grain material appears to be similar, the dissimilar JWST colors and dust characteristics (e.g., grain size, relative grain abundance) support the distinct nature of these circumstellar clouds (I. De Looze et al. 2024, in preparation). The absence of any detected QSFs—as traced by NIR [Fe II] 1.644 μm line emission (B.-C. Koo et al. 2023) or optical Hα and [N II] $\lambda\lambda$6548, 6583 line emission (S. van den Bergh & K. Kamper 1985)—suggests that the CSM toward the north, east, and west of Cas A is less dense, as already suggested by

B.-C. Koo et al. (2023). Analyses of the X-ray spectra also suggest that the GM has elevated densities compared to the circumstellar dust in the north (J. Vink et al. 2024).

5.2. Highly Asymmetric Mass Loss

Based on the accompanying X-ray analysis (J. Vink et al. 2024), we argue that the QSFs and GM are located in front of Cas A. With no evidence for a counterpart behind Cas A, based on the lack of similar interactions on the rear side, this would require highly asymmetric mass loss from the progenitor star. This argument is further supported by hydrodynamic simulations that show evidence of the interaction of Cas A with an asymmetric dense circumstellar shell on the blueshifted nearside of the remnant (S. Orlando et al. 2022). There is little evidence of single stars experiencing significant asymmetric mass loss (see examples in N. Smith et al. 2001; M. Montargès et al. 2021; R. M. Humphreys & T. J. Jones 2022). Hence, a binary scenario may be required to account for the highly asymmetric one-sided mass loss that would have produced the observed distribution of the GM and the QSFs (see also B.-C. Koo et al. 2023). The one-sided mass loss may point to specific mass-loss scenarios, like eccentric orbits or sudden mass loss instead of smooth Roche lobe overflow in a binary system (e.g., R. M. Lau et al. 2022; C. Landri & O. Pejcha 2024). However, it is important to note that the asymmetric mass loss observed in some asymptotic giant branch stars and RSGs (N. L. J. Cox et al. 2012) has been attributed to alternative explanations, including large convective cells (J. Lim et al. 1998). Since deep searches have failed to detect a surviving companion star for Cas A, and this has been interpreted as evidence that the binary progenitor system of Cas A merged prior to the SN explosion (C. S. Kochanek 2018; W. E. Kerzendorf et al. 2019), there may be a connection between this merger phase and the extremely dense mass-loss phase associated with the GM and the QSFs. A similar merging scenario has been suggested for SN 1987A's preexplosion stellar evolution (T. Morris & P. Podsiadlowski 2007). However, the mass loss in SN 1987A's merging progenitor system resulted in a more or less axially symmetric mass distribution, not one-sided akin to the mass loss observed in Cas A's progenitor system. In planetary nebulae, highly asymmetrical mass loss with one side much denser than the other is attributed to triple-star interaction (e.g., Bear & Soker 2017). Future observations and numerical modeling will be crucial to study the complex nature of the Cas A progenitor system and to unravel the origin of the highly asymmetric mass-loss phase that resulted in the formation of the QSFs and GM.

6. Conclusions

Extensive mapping of Cas A with JWST reveals a unique structure seen in projection toward the center that is pockmarked with dozens of $1''$–$3''$ sized circular holes surrounded by rings of enhanced emission (D. Milisavljevic et al. 2024). The green color in multiband JWST imaging (originating from MIRI/F1130W and F1280W emission) makes this GM stand out from the remnant's other emission components. We present a multiwavelength view, including JWST NIRCam (F162M, F356W, and F444W) and MIRI imaging of the entire GM structure and NIRSpec and MRS

spectroscopic observations of a specific ring region, which allows an in-depth study of the origin of the GM emission.

We find that the GM corresponds to dusty CSM located on the nearside of Cas A that has been impacted by the forward shock. The detection of emission lines such as Brα 4.05 μm in the NIRSpec spectra and [Ne II] 12.81 μm, [Ne III] 15.56 μm, and [Fe II] 17.94 μm in the MIRI MRS spectra coinciding with part of the ring structure is consistent with a circumstellar origin. The low radial velocities inferred for these lines—ranging between -50 and $0\,\mathrm{km\,s^{-1}}$—provide additional evidence that we are tracing CSM. The distribution of dense circumstellar clumps—better known as QSFs—are in general alignment with the GM's location.

The analysis of X-ray data in a companion paper (J. Vink et al. 2024) further corroborates this scenario, finding similarity between the X-ray spectra in the GM and in previously identified shocked circumstellar dust clumps south of Cas A. The blueshift of the X-ray emission furthermore suggests that the interaction with the SN blast wave happens on the nearside of the remnant, which is consistent with the domination of negative radial velocities of the QSFs (B.-C. Koo et al. 2018).

The most striking and unexpected features of the GM are the numerous small circular holes that are distributed unevenly across the circumstellar structure. We believe the holes were created upon interaction of ejecta with CSM seen as the GM feature in colored JWST images. However, the exact timing for these interactions remains unclear. The impact of fast-moving ejecta knots could have taken place several tens of years prior to the forward shock impact. Upon impact, these knots would instigate shock or compression waves in the perpendicular direction from the ejecta knots' motions with CSM piling up and creating the (partial) ring structures. The obvious candidates capable of piercing through dense layers of circumstellar dust are Cas A's N-rich ejecta knots that move with fairly uniform space velocities of 8000–10,500 $\mathrm{km\,s^{-1}}$ and appear to have been ejected nearly isotropically from the explosion center (R. A. Fesen 2001; M. C. Hammell & R. A. Fesen 2008).

Alternatively, protrusions in the remnant's expanding ejecta can create holes in circumstellar shells soon after the impact by the forward shock due to ejecta "fingers" created through hydrodynamical instabilities that extend from the ejecta through the contact discontinuity to the shocked CSM, as demonstrated in recent numerical simulations (S. Orlando et al. 2022). Future observations and simulation efforts are needed to constrain the exact mechanism and formation timescale for these holes.

The detection and characterization of the GM structure with JWST provides further evidence for a highly asymmetric mass-loss episode in Cas A's progenitor star shortly (3×10^4–10^5 yr) before the explosion. This conclusion is in line with previously identified shocked dense circumstellar QSFs (B.-C. Koo et al. 2023). The GM and QSFs share several characteristics, which may suggest that these dense CSM structures also share a common mass-loss phase experienced by Cas A's progenitor star. Future JWST/NIRSpec MSA spectroscopic observations for a variety of GM and QSF regions will be crucial to gain insights into the velocity structure, the physical properties, and the elemental abundances of this new CSM component to understand the late evolutionary phases of the Cas A progenitor mass loss prior to its explosion.

Appendix
Spectral Decomposition

A.1. Line Profile Analysis

We present an overview of the spectral decomposition of the NIRSpec and MIRI/MRS spectra in different velocity components for each of the bright lines (see Figure 5) detected in the MIRI MRS pointing targeting a bright ring in the GM. To limit the contamination by other velocity components, we extracted the emission from a $2\rlap{.}''5 \times 2\rlap{.}''5$ box centered on the ring. The ejecta-dominated lines ([S IV] 10.51 μm, [S III] 18.71 μm, and [O IV] 25.89 μm) show several velocity components ranging between -5000 and $+5000\,\mathrm{km\,s^{-1}}$. For sulfur, the brightest lines are blueshifted with radial velocities ranging between -2500 and $0\,\mathrm{km\,s^{-1}}$. There is a good correspondence between the velocity components detected in both sulfur lines. The predominance of blueshifted components may reflect asymmetries in the explosion and/or could be the

consequence of shock interactions on the nearside of Cas A due to a dense CSM that has created a reverse shock early on that is currently interacting with the expanding ejecta. For the redshifted velocity components, there are peaks around +950, +1550, +4000, and +4400 km s^{-1} for the sulfur and oxygen lines. The oxygen line profile shows a very prominent line around ∼+5000 km s^{-1} without any associated sulfur emission but does show [Ne II], [Ne III], and [Ne V] line emission at those velocities that is spatially coincident with a high-velocity ejecta filament that runs up against the base of the ring structure (see Figure 11). The absence of any obvious sulfur line emission corresponding with this high-velocity ejecta filament may suggest that it originates from the O/Ne layer of the progenitor star, whereas the other ejecta filaments instead originate from layers where there has been mixing between the O/Ne and Si/S layers. Apart from this high-velocity ejecta filament, there is excellent correspondence between the S and O line velocity components, which leaves little room for a contribution from the [Fe II] 25.99 μm line. We stress that it is unlikely for the [Fe II] 25.99 μm line to contribute significantly to the $v = 5000$ km s^{-1} velocity component due to the absence of any other iron line emission ([Fe II] 17.93 μm, [Fe III] 22.93 μm) at those high velocities within the MIRI MRS wavelength coverage.

Although the MIRI MRS cubes have been background-subtracted, there is a preponderance of near-rest-frame H$_2$ line emission across the entire MIRI MRS field of view that seems unrelated to any of the ejecta and/or circumstellar velocity components. These H$_2$ lines map out the warm interstellar medium on the line of sight to Cas A. The detection of warm H$_2$ emission requires shock excitation or UV pumping for the material to reach temperatures of several hundred kelvins.

Another near-rest-frame velocity component traces quasi-stationary CSM emitting brightly in several Ne ([Ne II] 12.81 μm and [Ne III] 15.56 μm), Fe ([Fe II] 1.644 μm and [Fe II] 17.93 μm), and hydrogen recombination (Brα 4.05 μm[36]) lines. There is a tentative detection of [Ne V] 14.32 μm line emission (see Figure 5) near-rest-frame wavelengths, but the offset in the line emission's spatial distribution and velocity (-220 km s^{-1}) warrants further investigation into the origin of this faint [Ne V] line emission. This near-zero km s^{-1} velocity component originates from a partial ring that closely resembles the morphology of the ring visible in the dust continuum maps (see Figure 12).

A.2. Line Modeling

Due to the complexity of the JWST/MIRI MRS spectra with a lot of material along the central lines of sight in Cas A, we fit a number of Gaussian profiles to disentangle the emission of different velocity components. We start by defining line-free wavelength ranges on either side of the line emission and fit a first-order polynomial to subtract the underlying continuum emission. We fit a minimum number of Gaussian components (i.e., one for each velocity component). The best-fit parameters for each Gaussian profile are determined based on a χ^2 minimization routine. The line flux in each spaxel is calculated as the flux integrated over the best-fit Gaussian profile. The radial velocity is calculated based on the Doppler velocity shift of the line center with respect to the rest-frame wavelength in vacuum, whereas the FWHM line width is calculated from the

---

[36] Note that other rings in the GM also emit in Hα (see Figure 4).

Table 1
Line-fitting Results for GM Ring in P2

Line	Rest-frame Wavelength (μm)	Line Intensity (10^{-16} erg s^{-1} cm^{-2})	Line Velocity (km s^{-1})	FWHM Line Width (km s^{-1})
[Fe II]	1.644	⩽1.25	…	…
Brα	4.05	0.29 ± 0.04	−19	226
[Fe II]	5.34017	⩽8.3	…	…
[Ne II]	12.81355	5.0 ± 0.2	−24	132
[Ne III]	15.55505	4.4 ± 0.3	−44	125
[Fe II]	17.93603	0.8 ± 0.2	−42	84
[Fe III]	22.9250	⩽3.0	…	…
[O IV]	25.8903	⩽5.2	…	…

Note. Near-rest-frame velocity line fluxes, heliocentric radial velocities, and FWHM of the emission lines showing a resemblance to the GM ring targeted with the NIRSpec and MRS observations in P2 (see Figure 1). In case of a nondetection, we quote 3σ upper limits. Note that the quoted line fluxes have not yet been corrected for dust extinction. The rest-frame wavelength in vacuum was adapted from the JWST line list (see https://pdrs4all.org/seps/#line-list).

best-fit Gaussian width parameter σ. To calculate the upper limits, we measure the 1σ standard deviation in a line-free region of the spectrum and calculate the upper limit as the flux integrated over a Gaussian profile with width similar to the other detected lines in that wavelength range and with amplitude equal to 3× the standard deviation σ. We followed this procedure for all lines associated with the quasi-stationary (near-zero velocity) CSM component that we identified as the GM. Table 1 summarizes the measured line fluxes, heliocentric line velocities, and FWHM line widths. Note that we calculated upper limits for the [S IV], [S III], and [O IV] line fluxes, even though there is emission detected around 0 km s^{-1}, since this emission seems unrelated to the GM ring detected in the dust continuum.

The [Fe II] 1.644 μm line flux is inferred from the NIRCam/F162M image using a rather complex procedure. All NIRCam images were first background-subtracted. We then isolated the ring, extracting the emission within an annulus with inner and outer radii of 0.″4 and 0.″6. We estimated the general background emission from a diffuse synchrotron background using the emission inside the ring. After subtracting this diffuse synchrotron background component, the residual emission will have contributions from synchrotron radiation (as detected in the ring structure in the NIRCam/F356W and F444W images) and from the [Fe II] 1.644 μm line emission. To calculate the contribution from synchrotron radiation within the ring, we measured the fluxes for the GM ring in the NIRCam/F356W and F444W images within the same annulus (after subtracting a diffuse synchrotron background) and fitted a power-law spectrum with $\alpha = -0.60$ (i.e., the mean value from V. Domcek et al. 2021 for this region) to these fluxes. Convolving this power-law spectrum with the JWST/NIRCam filters, we estimate the contribution from synchrotron emission within the ring, which is subtracted to obtain the residual [Fe II] line emission. Using the F356W flux to estimate the synchrotron contribution in the F162M filter, we are left with a flux of 1.25×10^{-16} erg s^{-1} cm^{-2} before applying any dust extinction correction. Extrapolation from the F444W flux for the ring
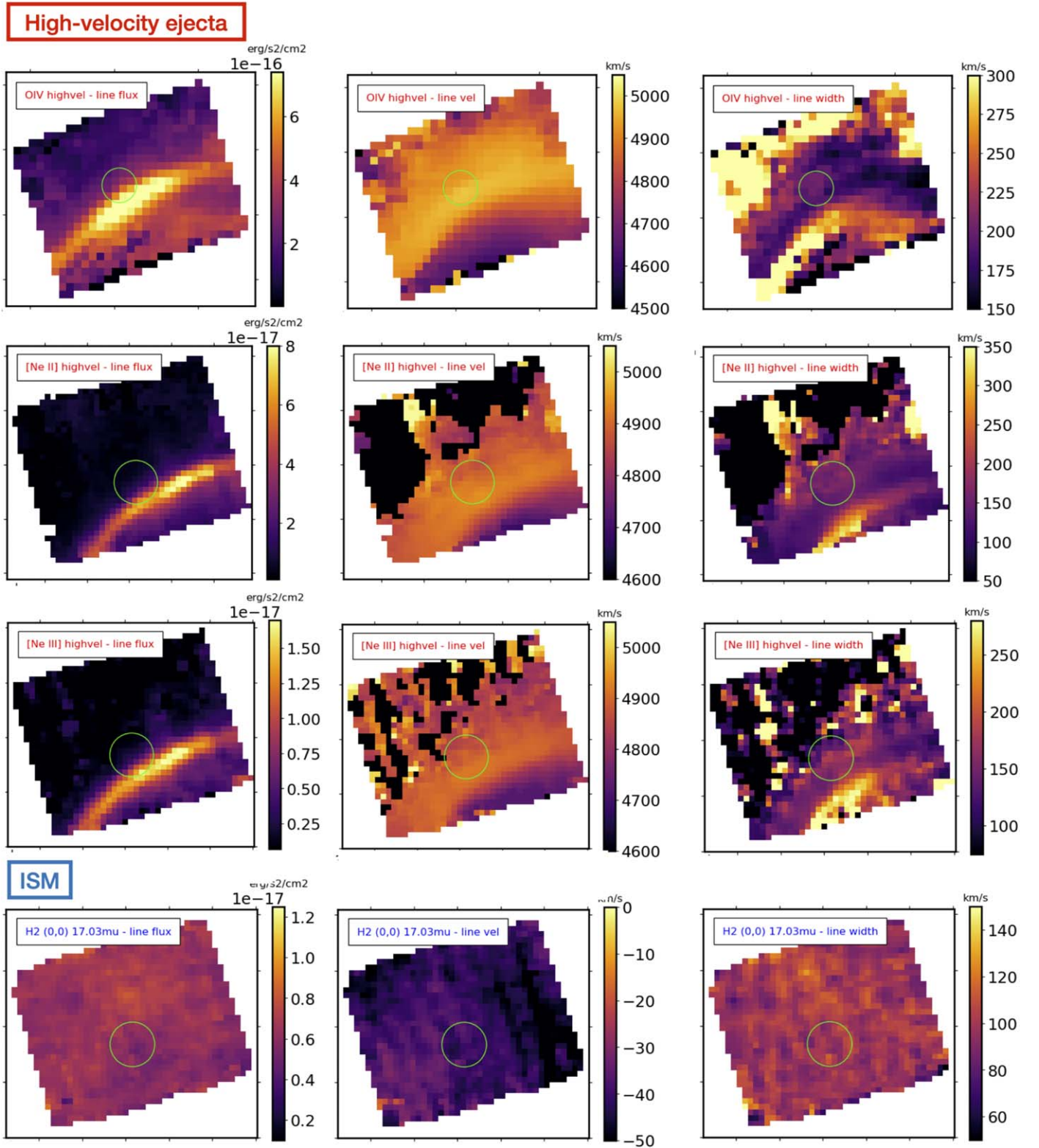
Figure 11. Spectral mapping of the GM ring region in position P2 (see Figure 1) for the high-velocity ($v = 5000$ km s^{-1}) ejecta component (top row) and the stationary ISM component (bottom row). For the high-velocity ejecta component, maps are shown of the line flux (left column), line velocity (middle column), and FWHM line width (right column) for the [O IV] 25.89 μm (first row), [Ne II] 12.81 μm (second row), and [Ne III] 15.56 μm (third row) lines. The line flux, line velocity, and line width maps of the H$_2$ (0, 0) 17.03 μm line of interstellar origin are shown in the bottom panels. The green circle roughly outlines the position of the ring in MIRI dust continuum maps (see Figure 7) and is overlaid on the line maps to guide the eye.

results in a high predicted synchrotron flux in the F162M filter, making it debatable whether or not there is any residual Fe line emission originating from the NIRCam/F162M image. It is

likely that other contributions to the F444W emission (e.g., hot dust emission) may cause these high synchrotron flux estimates. Given the many uncertain factors (i.e., the normalization and
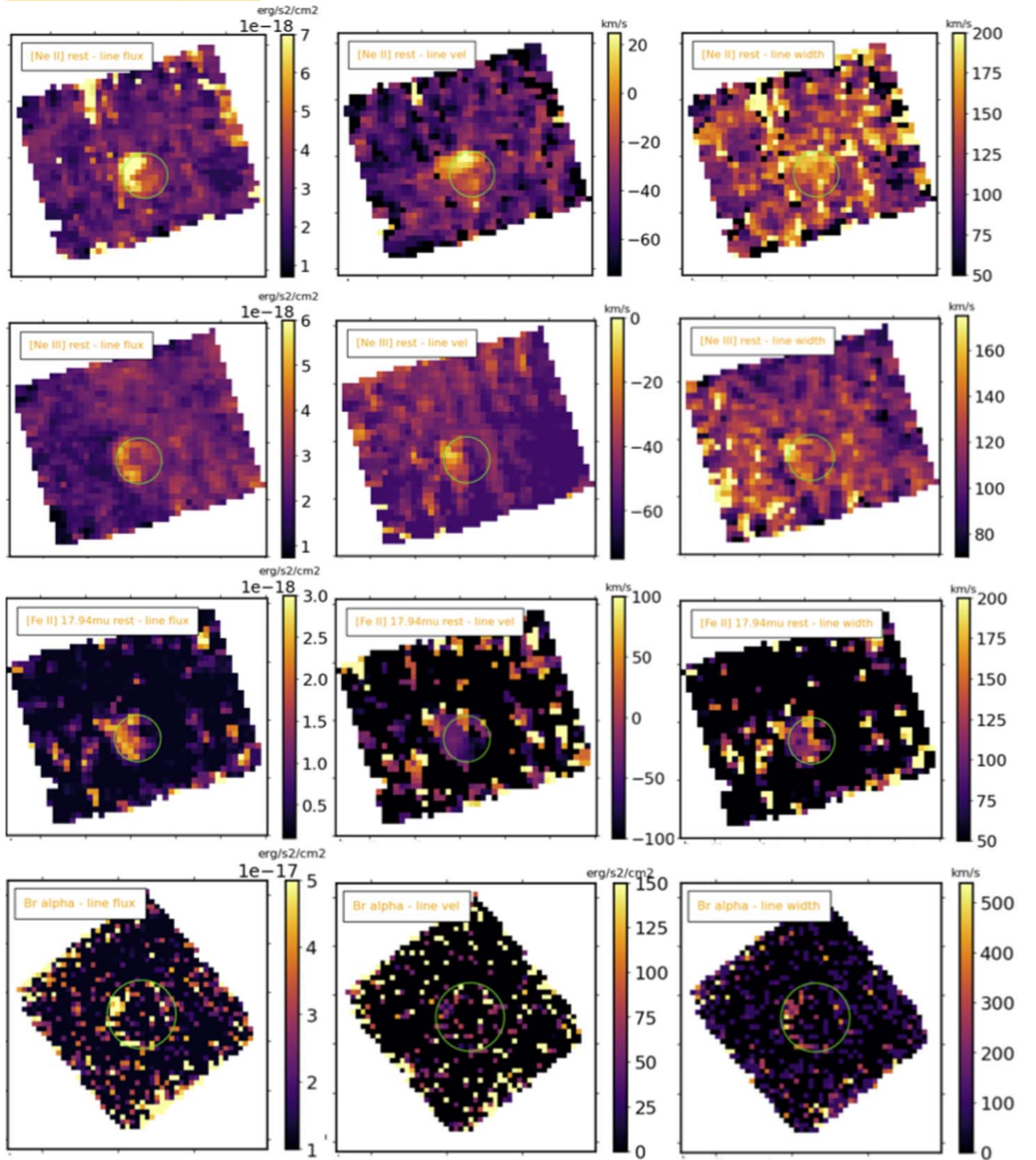
Figure 12. Spectral mapping of the GM ring region in position P2 (see Figure 1) near-rest-frame velocities. Maps are shown of the line flux (left column), line velocity (middle column), and FWHM line width (right column) for low-velocity components of the [Ne II] 12.81 μm (first row), [Ne III] 15.56 μm (second row), [Fe II] 17.94 μm (third row), and Brα (fourth row) lines. The green circle roughly outlines the position of the ring in MIRI dust continuum maps, with the same circle overlaid on the GM images shown in Figure 7.

power-law spectrum of the diffuse background, local synchrotron components, and dust extinction corrections) and the unavailability of NIRSpec data covering the [Fe II] 1.644 μm line, we consider the inferred [Fe II] 1.644 μm flux using the extrapolation of the F356W flux to estimate the synchrotron contribution as an upper limit. We require short-wavelength NIRSpec data in future JWST cycles in order to gauge the contributions of synchrotron emission and other [Fe II] lines (i.e., 1.599, 1.664, and 1.677 μm lines) that could also make substantial contributions to the F162M filter band (B.-C. Koo et al. 2016).

Finally, we need to consider dust extinction corrections for some of the lines. Due to the dense column of interstellar material toward the line of sight to Cas A, the visual extinction ranges between A_V of 7.5 and 15 mag (I. De Looze et al. 2017), depending on the specific sight line. Following the methodology of B.-C. Koo et al. (2018), we estimate a visual extinction of $A_V = 9.36$ mag from the column density map of U. Hwang & J. M. Laming (2012) and assuming $N_H/A_V = 1.87 \times 10^{21}$ cm^{-2} mag^{-1}. This translates into $A_{1.644} = 1.73$ mag assuming $A_{1.644}/A_V = 1/5.4$ (B. T. Draine 2003), suggesting that we need to correct our [Fe II] 1.644 μm flux by a factor of 5. In a similar way, the Brα emission is corrected for dust extinction assuming $A_{4.05} = 0.044$ mag.

ORCID iDs

Ilse De Looze https://orcid.org/0000-0001-9419-6355
Dan Milisavljevic https://orcid.org/0000-0002-0763-3885
Tea Temim https://orcid.org/0000-0001-7380-3144
Danielle Dickinson https://orcid.org/0000-0003-0913-4120
Robert Fesen https://orcid.org/0000-0003-3829-2056
Richard G. Arendt https://orcid.org/0000-0001-8403-8548
Jeremy Chastenet https://orcid.org/0000-0002-5235-5589
Salvatore Orlando https://orcid.org/0000-0003-2836-540X
Jacco Vink https://orcid.org/0000-0002-4708-4219
Michael J. Barlow https://orcid.org/0000-0002-3875-1171
Florian Kirchschlager https://orcid.org/0000-0002-3036-0184
Felix D. Priestley https://orcid.org/0000-0002-5858-6265
John C. Raymond https://orcid.org/0000-0002-7868-1622
Jeonghee Rho https://orcid.org/0000-0003-3643-839X
Nina S. Sartorio https://orcid.org/0000-0003-2138-5192
Tassilo Scheffler https://orcid.org/0009-0002-3600-4516
William P. Blair https://orcid.org/0000-0003-2379-6518
Ori Fox https://orcid.org/0000-0003-2238-1572
Christopher Fryer https://orcid.org/0000-0003-2624-0056
Hans-Thomas Janka https://orcid.org/0000-0002-0831-3330
Bon-Chul Koo https://orcid.org/0000-0002-2755-1879
J. Martin Laming https://orcid.org/0000-0002-3362-7040
Mikako Matsuura https://orcid.org/0000-0002-5529-5593
Dan Patnaude https://orcid.org/0000-0002-7507-8115
Mónica Relaño https://orcid.org/0000-0003-1682-1148
Armin Rest https://orcid.org/0000-0002-4410-5387
Judy Schmidt https://orcid.org/0000-0002-2617-5517
Nathan Smith https://orcid.org/0000-0001-5510-2424

References

Alarie, A., Bilodeau, A., & Drissen, L. 2014, MNRAS, 441, 2996
Allen, M. G., Groves, B. A., Dopita, M. A., Sutherland, R. S., & Kewley, L. J. 2008, ApJS, 178, 20
Arendt, R. G., Dwek, E., Kober, G., Rho, J., & Hwang, U. 2014, ApJ, 786, 55
Baade, W., & Minkowski, R. 1954, ApJ, 119, 206
Barlow, M. J., Krause, O., Swinyard, B. M., et al. 2010, A&A, 518, L138
Bear, E., & Soker, N. 2017, ApJL, 837, L10
Bevan, A., Barlow, M. J., & Milisavljevic, D. 2017, MNRAS, 465, 4044
Biscaro, C., & Cherchneff, I. 2016, A&A, 589, A132
Bocchio, M., Marassi, S., Schneider, R., et al. 2016, A&A, 587, A157
Braun, R., Gull, S. F., & Perley, R. A. 1987, Natur, 327, 395
Chevalier, R. A., & Kirshner, R. P. 1978, ApJ, 219, 931
Chevalier, R. A., & Oishi, J. 2003, ApJL, 593, L23
Cox, N. L. J., Kerschbaum, F., van Marle, A. J., et al. 2012, A&A, 537, A35
De Looze, I., Barlow, M. J., Swinyard, B. M., et al. 2017, MNRAS, 465, 3309
DeLaney, T., Rudnick, L., Stage, M. D., et al. 2010, ApJ, 725, 2038
Docenko, D., & Sunyaev, R. A. 2010, A&A, 509, A59
Domcek, V., Vink, J., Hernandez Santisteban, J. V., DeLaney, T., & Zhou, P. 2021, MNRAS, 502, 1026
Draine, B. T. 2003, ApJ, 598, 1017
Fesen, R., Patnaude, D., Milisavljevic, D., & Weil, K. 2019, in Supernova Remnants: An Odyssey in Space After Stellar Death II (Chania: NOA), 32
Fesen, R. A. 2001, ApJS, 133, 161
Fesen, R. A., Becker, R. H., & Blair, W. P. 1987, ApJ, 313, 378
Fesen, R. A., Hammell, M. C., Morse, J., et al. 2006, ApJ, 645, 283
Fesen, R. A., & Milisavljevic, D. 2016, ApJ, 818, 17
Fesen, R. A., Zastrow, J. A., Hammell, M. C., Shull, J. M., & Silvia, D. W. 2011, ApJ, 736, 109
Gardner, J. P., Mather, J. C., Abbott, R., et al. 2023, PASP, 135, 068001
Grefenstette, B. W., Harrison, F. A., Boggs, S. E., et al. 2014, Natur, 506, 339
Hammell, M. C., & Fesen, R. A. 2008, ApJS, 179, 195
Helder, E. A., & Vink, J. 2008, ApJ, 686, 1094
Hu, C.-Y., Zhukovska, S., Somerville, R. S., & Naab, T. 2019, MNRAS, 487, 3252
Humphreys, R. M., & Jones, T. J. 2022, AJ, 163, 103
Humphreys, R. M., Nichols, M., & Massey, P. 1985, AJ, 90, 101
Hwang, U., & Laming, J. M. 2009, ApJ, 703, 883
Hwang, U., & Laming, J. M. 2012, ApJ, 746, 130
Hwang, U., Laming, J. M., Badenes, C., et al. 2004, ApJL, 615, L117
Kamper, K., & van den Bergh, S. 1976, ApJS, 32, 351
Kerzendorf, W. E., Do, T., de Mink, S. E., et al. 2019, A&A, 623, A34
Kirchschlager, F., Schmidt, F. D., Barlow, M. J., De Looze, I., & Sartorio, N. S. 2023, MNRAS, 520, 5042
Kirchschlager, F., Schmidt, F. D., Barlow, M. J., et al. 2019, MNRAS, 489, 4465
Kochanek, C. S. 2018, MNRAS, 473, 1633
Koo, B.-C., Kim, D., Yoon, S.-C., & Raymond, J. C. 2023, ApJ, 945, 158
Koo, B.-C., Kim, H.-J., Lee, Y.-H., et al. 2018, ApJ, 866, 139
Koo, B.-C., Kim, H.-J., Oh, H., et al. 2020, NatAs, 4, 584
Koo, B.-C., & Park, C. 2017, in Handbook of Supernovae, ed. A. W. Alsabti & P. Murdin (Berlin: Springer), 161
Koo, B.-C., Raymond, J. C., & Kim, H. J. 2016, JKAS, 49, 109
Krause, O., Birkmann, S. M., Usuda, T., et al. 2008, Sci, 320, 1195
Lagage, P. O., Claret, A., Ballet, J., et al. 1996, A&A, 315, L273
Lamb, S. A. 1978, ApJ, 220, 186
Laming, J. M., & Hwang, U. 2003, ApJ, 597, 347
Landri, C., & Pejcha, O. 2024, MNRAS, 531, 3391
Lau, R. M., Hankins, M. J., Han, Y., et al. 2022, NatAs, 6, 1308
Lawrence, S. S., MacAlpine, G. M., Uomoto, A., et al. 1995, AJ, 109, 2635
Lee, J.-J., Park, S., Hughes, J. P., & Slane, P. O. 2014, ApJ, 789, 7
Lim, J., Carilli, C. L., White, S. M., Beasley, A. J., & Marson, R. G. 1998, Natur, 392, 575
Micelotta, E. R., Dwek, E., & Slavin, J. D. 2016, A&A, 590, A65
Milisavljevic, D., & Fesen, R. A. 2015, Sci, 347, 526
Milisavljevic, D., Temim, T., De Looze, I., et al. 2024, ApJL, 965, L27
Minkowski, R. 1959, in IAU Symp. 1, Paris Symp. on Radio Astronomy, ed. R. N. Bracewell (Stanford, CA: Stanford Univ. Press), 315
Montargès, M., Cannon, E., Lagadec, E., et al. 2021, Natur, 594, 365
Morris, T., & Podsiadlowski, P. 2007, Sci, 315, 1103
Nomoto, K., Suzuki, T., Shigeyama, T., et al. 1993, Natur, 364, 507
Orlando, S., Wongwathanarat, A., Janka, H. T., et al. 2021, A&A, 645, A66
Orlando, S., Wongwathanarat, A., Janka, H. T., et al. 2022, A&A, 666, A2
Peimbert, M., & van den Bergh, S. 1971, ApJ, 167, 223
Priestley, F. D., Arias, M., Barlow, M. J., & De Looze, I. 2022, MNRAS, 509, 3163
Reed, J. E., Hester, J. J., Fabian, A. C., & Winkler, P. F. 1995, ApJ, 440, 706
Rest, A., Foley, R. J., Sinnott, B., et al. 2011, ApJ, 732, 3
Rest, A., Pierel, J., Correnti, M., et al. 2023, arminrest/jhat: The JWST HST Alignment Tool (JHAT), v2, Zenodo, doi:10.5281/zenodo.7892935
Rest, A., Welch, D. L., Suntzeff, N. B., et al. 2008, ApJL, 681, L81

Rho, J., Kozasa, T., Reach, W. T., et al. 2008, ApJ, 673, 271
Rho, J., Park, S. H., Arendt, R., et al. 2024, ApJL, 969, 13
Rieke, M. J., Kelly, D. M., Misselt, K., et al. 2023, PASP, 135, 028001
Rigby, J., Perrin, M., McElwain, M., et al. 2023, PASP, 135, 048001
Schure, K. M., Vink, J., García-Segura, G., & Achterberg, A. 2008, ApJ, 686, 399
Smith, N., Humphreys, R. M., Davidson, K., et al. 2001, AJ, 121, 1111
Smith, N., & Morse, J. A. 2004, ApJ, 605, 854
Thorstensen, J. R., Fesen, R. A., & van den Bergh, S. 2001, AJ, 122, 297
van den Bergh, S. 1971, ApJ, 165, 457
van den Bergh, S., & Dodd, W. W. 1970, ApJ, 162, 485
van den Bergh, S., & Kamper, K. 1985, ApJ, 293, 537

van den Bergh, S., & Kamper, K. W. 1983, ApJ, 268, 129
van Veelen, B., Langer, N., Vink, J., García-Segura, G., & van Marle, A. J. 2009, A&A, 503, 495
Vink, J., Agarwal, M., Slane, P., et al. 2024, ApJL, 964, L11
Vink, J., Patnaude, D. J., & Castro, D. 2022, ApJ, 929, 57
Weil, K. E., Fesen, R. A., Patnaude, D. J., et al. 2020, ApJ, 891, 116
Wongwathanarat, A., Janka, H.-T., Müller, E., Pllumbi, E., & Wanajo, S. 2017, ApJ, 842, 13
Woosley, S. E., & Weaver, T. A. 1995, ApJS, 101, 181
Wright, G. S., Rieke, G. H., Glasse, A., et al. 2023, PASP, 135, 048003
Young, P. A., Fryer, C. L., Hungerford, A., et al. 2006, ApJ, 640, 891